

MODELS FOR THE COMBUSTION OF INDIVIDUAL PARTICLES OF VARIOUS COAL TYPES

Chun Wei Lau and Stephen Niksa*
High Temperature Gasdynamics Laboratory
Stanford University, Stanford, CA 94305

Keywords: Modeling, coal combustion, soot, coal type effects

INTRODUCTION

Our modeling aims to identify the chemical processes and transport mechanisms underlying differences in the ways that different types of coal burn. At this point, thermal histories and audits of the heat release from individual particles are emphasized. Three limiting cases have been formulated for this comparative study. In one scenario, the noncondensable gases and tars from primary devolatilization are consumed by combustion in envelope diffusion flames around individual particles. The devolatilization products from different coals are distinguished by different evolution rates, elemental compositions, average molecular weights, and transport properties. In another modeling scenario, the products of primary devolatilization are radically transformed by secondary pyrolysis after they are expelled from the coal until only H_2 , CO , C_2H_2 , CO_2 , H_2O , and soot remain. This scenario also develops separate limiting behavior for instantaneous soot oxidation in envelope flames and for frozen soot oxidation chemistry. Thermophoresis and radiation are accounted for in this transport analysis. Comparisons among predicted and observed flame lifetimes and maximum flame standoff distances indicate that transport-limited oxidation of secondary pyrolysis products, including soot, is the most realistic modeling scenario.

DESCRIPTION OF THE MODELS

Formal developments of all 3 models are available (1,2). The model that describes tar and gas combustion is denoted by FSCM-FSP for "Flame Sheet Coal Combustion Model with Frozen Secondary Pyrolysis." The two models with soot instead of tar are denoted by FSCM-ISP/ISO and FSCM-ISP/FSO where "ISP" denotes infinitely-fast secondary pyrolysis, and the modifiers "ISO" and "FSO" denote infinitely-fast and frozen soot oxidation, respectively. All scenarios account for primary devolatilization (with FLASH2 (3)), multicomponent diffusion and Stefan flow, fuel accumulation between the particle surface and flame sheet, instantaneous volatiles combustion, and heterogeneous oxidation of char into CO . The common heat transfer mechanisms are the fuel particle's thermal capacitance and radiation flux, heat conduction from the particle and flame, advection of sensible enthalpy, and the heats of pyrolysis, char oxidation, and volatiles combustion. Flame temperatures and the distribution of combustion products are based on thermochemical equilibrium among 12 species, including dissociation fragments.

Both of the FSCM-ISP models invoke infinitely-fast conversion of tar into soot, so only soot and noncondensibles are ejected from the particle into the gas film. The elements in tar are apportioned into soot having a C/H ratio of 9, the ultimate value for any coal type, and appropriate amounts of H_2 and CO . Noncondensibles compositions are adjusted further to eliminate the amount of C_2H_2 that maintains equal masses of soot and tar, consistent with recent laboratory studies. Soot's Brownian diffusivity is considerably lower than tars', and the inverted temperature profile from particle to flame drives thermophoresis that counteracts its Brownian and convective transport.

*Current address: Molecular Physics Laboratory, SRI International
333 Ravenswood Avenue, Menlo Park, CA 94025

RESULTS

As fuels, soot and noncondensable gases from different coals have the characteristics in Table 1. Total weight loss tends to be the same for all ranks through hv bituminous then falls off for medium and low volatile bituminous coals, and vanishes for anthracites. Yields of noncondensibles decrease monotonically with rank, so soot yields are maximized with hv bituminous samples. The stoichiometric ratios and lower heating values of soot from the four coal types mimic the trends in tar characteristics, but values for soot are higher. The stoichiometry for gas combustion increases with rank, reflecting less dilution by CO_2 , H_2O , and other oxygenated species.

Temperature histories and flame trajectories from all 3 models appear in Fig. 1. These simulations are for 70 μm Pit. #8 particles injected into a stream of 8% O_2 in N_2 at 1500 K within a conduit at 900 K. When sooting is ignored, flame temperatures (Fig. 1a) reach the hottest maximum value (2600 K) because tar/gas flames penetrate furthest into the film (Fig. 1b). Soot/gas flames are much cooler, reaching only 2320 K, and stay closer to their particles. Note, however, the particle heating rate from FSCM-ISP/ISO is substantially higher than from FSCM-FSP, by virtue of radiation from soot to the particle. Flames from FSCM-ISP/ISO last longer than from FSCM-FSP, even though the particle heating rates from FSCM-ISP/ISO are faster. Clearly, radiation from soot to the particle is also significant, accounting for up to one-third of the conduction flux to the particle at the point of maximum flame standoff. On a cumulative basis, 12% of the heat of volatiles combustion is radiated back to the particle.

Calculations from FSCM-ISP/FSO which omit soot oxidation predict much cooler temperature histories for flames and particles (Fig. 1a). Because of their low oxygen requirements, gas flames sit close to the particle, penetrating only up to 4 radii into the film, and have the shortest pathway for conductive feedback. Also, the extent of the soot layer increases without bound when soot survives the flame, so radiation losses also grow continuously. Consequently, the flame temperature from FSCM-ISP/FSO reaches the implausibly low value of 1800 K.

With the FSCM-ISP models, macroscopic features of the Pit. #8 are fairly representative of the other coal types. Maximum flame temperatures in Table 2 vary by less than 200 K. Qualitatively, the same rank-dependence is seen with FSCM-FSP. But quantitatively, sooting suppresses the rank dependence because soot radiation is strongest for coals with the largest soot yields. Soot radiation cools flames on Pit. #8 particles by 300 K, but for Zap and Poc. coals the reduction is only 200 K, so differences are reduced. Flame radii also become more insensitive to coal rank when sooting is included.

Because of their similar flame temperatures, audits of the energy release based on FSCM-ISP/ISO are also similar for all coal types. For 100 μm particles, roughly one-third is transferred into the surroundings while 60% is radiated or conducted back to the particle. Only a few percent is carried away by intermediate species. Since flame standoffs depend on particle size, the fractional energy feedback to the particle is also size-dependent. For sizes larger than the threshold for attached flames, the fraction feedback increases for smaller sizes, exceeding 90% at the critical size for all coal types. The critical sizes for heterogeneous combustion indicate the size at which oxygen transport is fast enough to consume all volatiles and oxidize the char on the particle surface, in an "attached" flame. These values are virtually identical for all 3 models.

Only flame durations and maximum standoffs monitored in a drop tube furnace (4) are available to evaluate the different modeling scenarios. Actual particle sizes, coal properties, gas temperatures, and O_2 levels are used in the simulations, but none of the modeling parameters were adjusted or specified to improve the fit of the model predictions. Observed flame durations are plotted with predictions for Ill. #6 coal in Fig. 2a. Predictions from FSCM-FSP and FSCM-ISP/ISO are within experimental

uncertainty, but those from FSCM-ISP/FSO are too long at all O_2 levels. The evaluation of flame standoffs for the same coal appears in Fig. 2b. Here differences among the 3 models are somewhat more discriminating. Predicted standoffs from SFCM-ISP/ISO provide the closest match, although FSCM-FSP/FSO predictions are also within experimental uncertainty. But FSCM-ISP/FSO predictions are much too low.

DISCUSSION

These simulations are the basis for several recommendations regarding models to predict the macroscopic combustion characteristics of the initial stages of pulverized coal combustion. Flame durations are governed by the evolution of primary devolatilization products, not heat or mass transport, and flame trajectories and maximum standoffs are primarily governed by the stoichiometric oxygen requirements of the fuel and fuel species accumulation. So these aspects are insensitive to soot formation. Likewise, the ways that particle sizes and the oxygen levels and temperatures in the free stream affect combustion characteristics are also insensitive to sooting. In contrast, reliable flame temperatures and concentration and temperature profiles can only be computed from models that account for the radiation heat transfer and thermophoretic mass transfer of soot. Although we have not yet expanded this model to represent NO_x formation, it is worth noting that the fuel species concentration profiles between particle surfaces and flame sheets are also significantly affected by thermophoretic and Brownian transport of soot. Both of these mechanisms enhance the accumulation of soot in the film, thereby flattening the fuel concentration profiles throughout.

REFERENCES

1. Lau, C.-W., and Niksa, S., *Combust. Flame*, 1992, **90**, 45.
2. Lau, C.-W., and Niksa, S., *Combust. Flame*, 1993, to appear.
3. Niksa, S., *AIChE J.*, 1988, **43**, 790.
4. Timothy, L. D., Froelich, D., Sarofim, A. E., Beer, J. M., Twenty-First Int. Symp. on Combust., 1986, 1141, The Combustion Institute, Pittsburgh, PA.

Table 1. Combustion Characteristics of Secondary Pyrolysis Products From Four Coals.

	Zap	Ill. #6	Pit. #8	Poc.
Ultimate Yield, wt. % daf				
Soot	20.4	26.7	35.7	15.5
Gases	33.3	25.3	19.0	8.3
Molar Stoichiometry				
Soot Combustion	36.5	31.6	27.9	25.6
Gas Combustion	0.33	0.80	0.83	1.10
ΔH_C°, kJ/mole				
Soot	1.5×10^4	1.4×10^4	1.3×10^4	1.2×10^4
Gases	3.4×10^2	4.9×10^2	5.0×10^2	5.6×10^2
All Volatiles	4.4×10^2	1.3×10^3	1.8×10^3	1.4×10^3

Table 2. Selected Combustion Characteristics For the Four Coals From FSCM-ISP/ISO.

	Zap	Ill. #6	Pit. #8	Poc.
Max. Flame Temp., K	2130	2190	2320	2160
Max. Flame Standoff, particle radii	5.4	6.0	7.0	5.8
Critical Sizes for Hetero. Combustion Mode, μm	18.2	15.8	8.0	27.8
Energy Fraction Feedback to Particle	0.61	0.62	0.56	0.64
Energy Fraction Lost to Free Stream	0.33	0.32	0.32	0.30

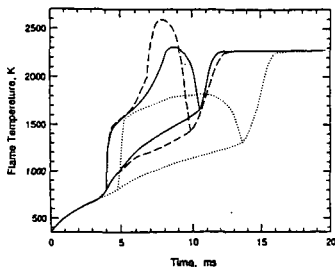


Fig. 1 (a) Transient particle and flame temperatures for base operating conditions based on FSCM-FSP (dashed curve) FSCM-ISP/ISO (solid curve) and FSCM-ISP/FSO (dotted curve).

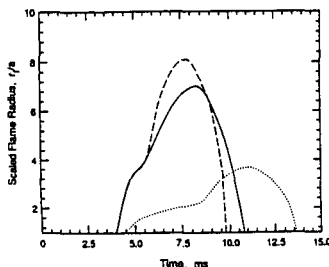


Fig. 1 (b) Flame trajectories based on FSCM-FSP (dashed curve), FSCM-ISP/ISO (solid curve), and FSCM-ISP/FSO (dotted curve).

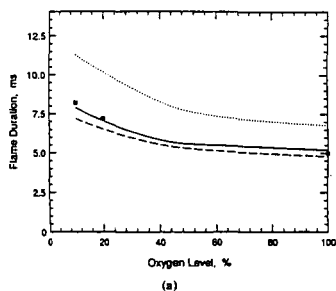


Fig. 2(a). Predicted flame durations for the Ill. #6 coal based on FSCM-FSP (dashed curve), FSCM-ISP/ISO (solid curve), and FSCM-ISP/FSO (dotted curve) compared to measured values [4] for a Utah hv bituminous coal of similar composition. At all oxygen levels, the size is 100 μm and the gas temperature is 1250 K.

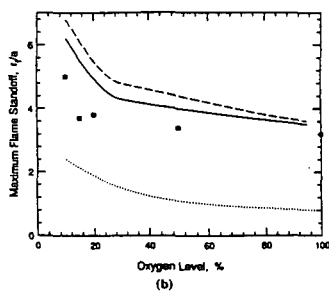


Fig. 2(b). Predicted maximum flame standoffs for the Ill. #6 coal based on FSCM-FSP (dashed curve), FSCM-ISP/ISO (solid curve), and FSCM-ISP/FSO (dotted curve) compared to measured values [4] for a Utah hv bituminous coal of similar composition. At all oxygen levels, the size is 100 μm and the gas temperature is 1250 K.

MODELING DEVOLATILIZATION RATES AND YIELDS FROM VARIOUS COALS WITH FLASHCHAIN

Stephen Niksa and Alan R. Kerstein
SRI International, Menlo Park, CA 94025 and
Sandia National Laboratories, Livermore, CA 94550

Keywords: Modeling, coal devolatilization, coal type effects

INTRODUCTION

Predicting the ultimate weight loss and tar yields from any coal type is largely a matter of distinguishing aliphatic, heteroatomic, and aromatic constituents. In FLASHCHAIN (1-3), this crucial partitioning is implemented with balances based on the ultimate analysis, carbon aromaticity, aromatic carbon number per monomeric unit, and other characterization data. This study shows that the ultimate analysis is the only sample-specific data needed for accurate predictions of ultimate tar and total yields with this theory, consistent with a previous parametric sensitivity study(3). Regression values of all other inputs are adequate. Along with evaluations of ultimate yields for coals across the rank spectrum, reliable transient predictions for rapid atmospheric devolatilization of any coal type are also demonstrated.

OVERVIEW OF THE THEORY

FLASHCHAIN invokes a new model of coal's chemical constitution, a four-step reaction mechanism, chain statistics, and the flash distillation analogy (4) to explain the devolatilization of various coal types. The theory's central premise is that the partitioning of the elements among aliphatic, heteroatomic, and aromatic constituents largely determines the devolatilization behavior of any coal type. The abundance of labile bridges in lignites promotes their extensive conversion to noncondensable gases, but their oxygen promotes the charring of bridges into refractory links, which inhibits fragmentation of the macromolecules into tar. Conversely, the paucity of labile bridges in low volatility coals suppresses gas yields. These coal also have too few labile bridges for extensive fragmentation, so their tar yields are also relatively low. High volatile bituminous coals generate an abundance of tar precursors, so a competition between flash distillation and repolymerization into larger, refractory fragments determines their tar yields.

Coal is modeled as a mixture of chain fragments ranging in size from a monomer to the nominally infinite chain. They are constructed from only four structural components: aromatic nuclei, labile bridges, char links, and peripheral groups. Aromatic nuclei are immutable units having the characteristics of the hypothetical aromatic cluster based on ^{13}C NMR analysis. They also contain all of the nitrogen in the coal. Nuclei are interconnected by two types of linkages, labile bridges or char links. Labile bridges are the key reaction centers. They represent groups of aliphatic, alicyclic, and heteroatomic functionalities, not distinct chemical bonds. Bridges contain all of the oxygen, sulfur, and aliphatic carbon, but no aromatic components. Being refractory, char links are completely aromatic with no heteroatoms. Peripheral groups are the remnants of broken bridges.

Connectedness among nuclei is another important aspect of coal rank. In FLASHCHAIN, the initial coal configuration is specified by the proportions of broken bridges and intact linkages. Since the number of linked nuclei denotes the fragment size, the fraction of broken bridges determines the initial fragment size distribution. This distribution is empirically related to extract yields in pyridine. Quali-

tatively, fragment distributions skewed toward smaller sizes correspond to coals with substantial amounts of readily extractable material.

All parameters in the constitution submodel are collected in Table 1 for diverse coal samples. Four are based on molecular weights: that of the aromatic nucleus, MW_A , is used to normalize those of labile bridges (MW_B/MW_A), char links (MW_C/MW_A), and peripheral groups (MW_P/MW_A). The tabulated values show that nuclei become more massive in coals of higher rank, and both the labile and refractory connections among them become smaller. The proportion of intact links in the whole coal, $p(0)$, follows the tendency in the pyridine extract yields to remain constant for ranks through hv bituminous. It then rises precipitously for coals of higher ranks, consistent with their smaller extract yields because structures which are more tightly interconnected have fewer smaller fragments to be extracted. The fraction of labile bridges among intact links, $F^b(0)$, decreases from its value of unity for lignites in proportion to the carbon content.

The selectivity coefficient between scission and spontaneous char condensation, v_B , also varies with rank. Since crosslink formation has been clearly related to CO_2 evolution, the values of v_B are proportional to O/C ratios, but only for values below 0.2 or for carbon contents less than 83%. The latter restriction is consistent with the fact that precursors to CO_2 are either carboxylic acid or ketone functionalities, which are present only in lower rank coals.

RESULTS

In the forthcoming simulations only the operating conditions of temperature, heating rate, and/or time were varied to match those in the experiments. A simulation of each thermal history requires from 2 to 5 minutes on a 386 personal microcomputer operating at 20 MHz with an 8-Bit Fortran compiler.

Figure 1 presents comparisons among the predicted and measured ultimate values of weight loss and tar yield based on the laboratory study of Xu and Tomita (5). The data are ultimate yields for atmospheric pyrolysis for a heating rate of 3000 K/s and a 4 s reaction time at 1037 K. The predicted weight loss is within 4 wt. % of the measured values in 13 of the 17 cases. The predictions also display the perturbations from a smooth, monotonic trend that is evident in the data. Similarly, predicted tar yields are within 4 wt. % of the observed values in 14 of the 17 cases, and also depict the rather erratic relation with carbon content that is observed. The only sample-specific inputs for these simulations are the reported ultimate analyses.

Weight loss and tar yields for transient devolatilization of 4 coal types throughout diverse thermal histories appear in Fig. 2. These cases represent ranks from subbituminous through lv bituminous. Throughout all of these cases, the FLASHCHAIN predictions are within experimental uncertainty.

Nominal devolatilization rates for 8 coals for atmospheric devolatilization at 10^4 K/s appear in Fig. 3. The curves are the rate constants in single first order reactions which match the FLASHCHAIN predictions. These simulations indicate that devolatilization occurs over a narrower temperature range for higher rank coals, although the variation is rather modest. Rate variations with rank segregate into two categories. For ranks from lignite through hv bituminous, rank variation are modest, especially during the later stages of devolatilization at high temperatures. Nominal rates for these ranks vary by a factor of 3 at 715 K, but by only 40% at 1000 K. The temperature at which devolatilization commences also varies, from 600 K for the lignite to 680 K for the hv bituminous coals. (Of course, these temperatures will shift for different heating rates.) Low volatility coals comprise the second category. They begin to devolatilize at much higher temperatures and sustain significantly slower rates than the other ranks. Even so, the variations among very diverse coal samples are never as substantial as those from varying the heating rate by a single order of magnitude.

DISCUSSION

This reaction model delivers reliable yields of gas and tar for any coal at any operating conditions, yet it requires only a few minutes per simulation on a personal microcomputer. Throughout the entire rank spectrum, this theory quantitatively represents observed yields using only the sample-specific ultimate analyses and regression values of all other input data. To date, predictions for some 40 different coal samples covering the entire rank spectrum have been evaluated against measured transient and/or ultimate yields. In all but a few cases, the model predictions are within experimental uncertainty. Transient cases in the evaluations are also satisfied. The predictions show that devolatilization rates are very insensitive to rank through hvA bituminous, but then fall off for low volatility coals.

REFERENCES

1. Niksa, S. and Kerstein, A. R., Energy Fuels, 1991, 5, 647.
2. Niksa, S., Energy Fuels, 1991, 5, 665.
3. Niksa, S., Energy Fuels, 1991, 5, 673.
4. Niksa, S., AIChE J., 1988, 34, 790.
5. Xu, W.-C. and Tomita, A., Fuel, 1987, 66(5), 627.
6. Xu, W.-C. and Tomita, A., Fuel, 1987, 66(5), 632.
7. Freihaut, J. D. and Proscia, W. M., Final Report on U. S. DOE Contract No. DE-AC22-89PC89759, 1991, Pittsburgh Energy Technology Center.
8. Oh, M.-S., Peters, W. A., and Howard, J. B., AIChE J., 1989, 35, 775.

Table 1. Structural Model Parameters

%C, daf	MW _A	C _A	MW _M / MW _A	MW _C / MW _A	MW _P / MW _A	p(0)	F _b (0)	v _B	v _E
66.5	125	9.7	1.859	.836	.511	.911	1.000	.150	2.40
69.0	134	10.6	1.602	.721	.442	.911	1.000	.150	2.23
69.5	135	10.7	1.563	.704	.430	.911	0.983	.150	2.19
74.1	148	11.6	1.307	.588	.359	.911	0.858	.329	2.03
75.5	152	11.9	1.258	.566	.347	.911	0.821	.202	2.05
79.9	165	12.9	1.044	.470	.288	.911	0.702	.370	2.00
82.5	176	13.7	0.901	.406	.247	.911	0.632	.500	1.93
84.0	180	14.1	0.838	.377	.230	.911	0.591	.500	1.90
87.4	169	13.4	1.079	.485	.297	.911	0.329	.500	2.48
87.5	182	14.2	0.886	.399	.243	.911	0.366	.500	2.19
88.7	183	14.4	0.866	.390	.239	.920	0.329	.500	2.21
89.6	186	14.6	0.836	.376	.230	.937	0.301	.500	2.21
89.9	181	14.4	0.897	.404	.247	.943	0.291	.500	2.33
94.3	178	14.5	1.005	.452	.097	1.000	0.154	.500	2.86

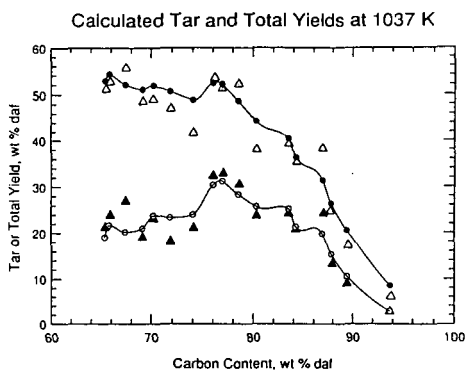


Figure 1. An evaluation of ultimate weight loss and tar yields for atmospheric devolatilization based on the study of Xu and Tomita (5). FLASHCHAIN predictions appear as the circles connected by solid lines, and the measured values appear as the contrasting triangles.

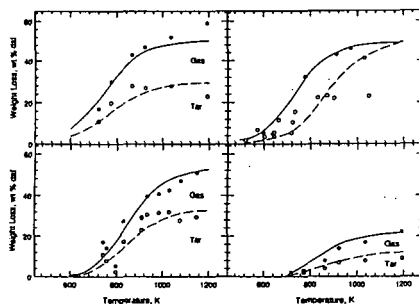


Figure 2. Representative FLASHCHAIN predictions for transient atmospheric devolatilization of four diverse coal types. (a) Total and tar yields from a subbituminous coal for 4 s isothermal reaction after heating at 3000 K/s to various temperatures, reported by Xu and Tomita (6). (b) Ultimate and transient weight loss from Ill. #6 for a heating rate of 1000 K/s reported by Freihaut and Proscia (7). (c) Transient total and tar yields from Pit. #8 during heatup at 1000 K/s and slow cooling from various temperatures, reported by Oh. et al. (8). (d) Same as (a) for a bituminous coal.

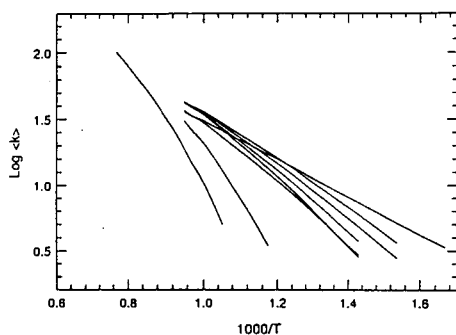


Figure 3. Arrhenius diagram of nominal devolatilization rates during transient heating at 10^4 K/s for the 8 coals tested by Xu and Tomita (6). In clockwise descending order, lines are for coals of increasing rank.

APPLICATION OF SEMI-GLOBAL HETEROGENEOUS MECHANISMS TO GRAPHITE OXIDATION IN A STAGNATION POINT FLOW

H.K. Chelliah

Department of Mechanical, Aerospace and Nuclear Engineering
University of Virginia
Charlottesville, VA 22903

Keywords: graphite oxidation, heterogeneous mechanisms, simulations

Introduction

Several reacting flow configurations have been used in previous experimental and theoretical studies to investigate the burning rate of graphite and its dependence on external flow fields. One commonly used method involves combustion of graphite particulates in a hot oxidizing environment, typically established by a fuel lean hydrocarbon-air flame.^{1,2} The analysis of gas samples for temperature and species concentration, the particle temperature and size histories have provided quantitative estimates for the surface regression rates and heterogeneous reaction rates. In another experimental method, hot graphite rods placed in a uniform cold oxidizing stream have been used to determine the heterogeneous reaction rates.³ Here the oxidizing stream conditions have been varied to study the effects of flow straining, oxidizer dilutions or enrichments, etc. In theoretical studies,^{1,4-10} semi-global reaction mechanisms have been commonly used to describe the heterogeneous graphite oxidation, while mechanisms ranging from global to detailed have been used for the homogeneous reactions. Although there have been recent efforts to implement elementary mechanisms for heterogeneous reactions, there are many uncertainties associated with the mechanisms and rate data employed.¹¹ Since the available rate data of the semi-global heterogeneous mechanisms can depend on physical properties of the graphite employed in experiments,¹²⁻¹⁴ there is a need to determine the validity of applying these rate data to different graphite shapes, sizes and reacting flow configurations. The objective of the present work is to perform such partial validations of semi-global heterogeneous rates through detailed numerical simulations.

The flow configuration adopted in the present numerical study corresponds to that of the graphite rod oxidation and is discussed below. Based on this flow configuration, comparisons of the burning rate predictions, the gas-phase flame structure and the variation of surface rates as a function of the surface temperature, strain rate, oxidizer concentration and pressure have been performed, but only selected results are presented here for brevity. Efforts are also underway to perform similar simulations of graphite particle oxidation in a quiescent atmosphere.

In addition to the kinetic effects on the graphite burning rate, the gas-phase *CO* flame extinction/ignition phenomena have been examined through numerical calculations. Instead of the experimentally observed extinction/ignition condition, under weak burning conditions the preliminary numerical results indicate a *CO* flame attachment/detachment phenomena.

Flow Configuration

The flow configuration used in the present numerical simulation is similar to that used in Ref. [15] and is shown in Fig. 1. The flow over the graphite rod is assumed to be steady, laminar and two dimensional. If x and y are the coordinates tangential and perpendicular to the graphite surface, respectively, and u and v are the corresponding velocity components, then the outer, inviscid, oxidizer flow can be described by $u_\infty = ax$ and $v_\infty = -ay$, where the subscript ∞ identifies the conditions in the outer flow and a is the velocity gradient in the oxidizer stream. The details of the formulation can be found in Refs. [16-18], the numerical procedure in Ref. [19], the thermodynamic data in Ref. [20], and transport data in Ref. [21]. Introducing the notation $f' = u/u_\infty$, the governing boundary layer equations for mass,

momentum, species and energy in the inner viscous region can be transformed into a system of ordinary differential equations along the stagnation-point stream line ($x=0$) and must be solved subject to the boundary conditions at the surface ($y = y_s$):

$$\begin{aligned} f' &= 0; \quad [\rho Y_i(v + V_i)]_s = \dot{s}_i, \quad i = 1, \dots, N; \\ T &= T_s; \quad (\rho v)_s = \sum_{i=1}^N \dot{s}_i, \end{aligned} \quad (1)$$

and at $y = y_\infty$:

$$f' = 1; \quad Y_i = Y_{i,\infty}, \quad i = 1, \dots, N; \quad T = T_\infty. \quad (2)$$

Here \dot{s}_i is the semi-global mass rate of production or consumption of the i th species by heterogeneous reactions at the surface, ρ is the density in the gas phase, T the temperature, Y_i the mass fraction of the i th species, and V_i the diffusion velocity of the i th species in y direction. In this formulation the burning rate of graphite is equivalent to $(\rho v)_s$. Subscript s identifies the properties at the surface. In the experiments of Makino et al. [3], the temperature of the graphite rod was maintained at a constant value with an external heating source during each burning rate measurement. Since the surface temperature is controlled, heat loss by radiation and heat released at the surface has no effect on T_s , hence the condition $T = T_s$ in Eq. (1) is applicable. However, in simulations of graphite particles in a hot oxidizing environment where such temperature control of the particle surface is absent, heat release by the surface reactions and also heat loss by radiation must be taken into consideration in order to evaluate the surface temperature accurately.¹¹ In all the numerical integrations reported here, the cold oxidizer temperature was set to the experimental condition of $T_\infty = 300$ K.

Reaction Mechanism

The surface reaction pathways have been extensively reviewed by Laurendeau [12] and Essenhigh [13], where it is shown that the overall carbon reactivity can be estimated by $R = \eta A_g \sum_i \dot{s}_i$. In the two heterogeneous reaction mechanisms listed in Tables 1A and 1B (which will be referred to as mechanisms A and B), the terms η (a measure of the species penetration into the solid) and A_g (internal surface area) have been absorbed into the frequency factors A_i and B_i .

The rate data of reactions A4 and A5 have been obtained from the experimental burning rate measurements of a graphite rod with a density of $\rho_c = 1.82 \times 10^3$ (kg/m³).³ The rate data of the remaining reactions, i.e. reaction of carbon with OH, O and H₂O in mechanism A are essentially the same as in B. The rate data of mechanism B have been compiled from various sources and are listed in Ref. [1]. Here, the thermal annealing effects have been included in the expression for the reaction $C + (1/2)O_2 \rightarrow CO$, significant only at temperatures above 2000 K. In addition, the data of reaction B5 are for pyrolytic graphite with small particle diameters having negligible internal mass transfer effects.

The gas-phase wet CO reaction mechanism is relatively well known and has been adopted from Yetter et al. [22]. The mechanism consists of 12 species in 28 elementary reactions and is shown in Table 2.

Results and Discussion

Figure 2 shows the predicted burning rate of a graphite rod as a function of surface temperature (T_s) using the two surface reaction mechanisms A and B. The water mass fraction of the oxidizing air stream was set to the experimental value of $Y_{H_2O} = 0.005$. The results with mechanism A are shown for two different strain rates, $a = 200$ s⁻¹ and 820 s⁻¹; experimental results of Makino et al. [3] are shown for comparisons. At low temperatures ($T_s < 1200$ K), the reactions A4 ($C_s + CO_2 \rightarrow 2CO$) and A5 ($2C_s + O_2 \rightarrow 2CO$) are insignificant because of their large activation energies. Furthermore, since there is no gas-phase reaction at these temperatures, radicals are almost non-existent so that the remaining reactions are also inactive. As T_s approaches 1300 K, reaction step A5 with an overall activation energy

of 43.0 kcal/mole becomes significant, leading to a rapid increase in the burning rate as seen in Fig. 2. With further increase in T_s , step A4 with relatively higher activation energy (64.3 kcal/mole) becomes important around $T_s \sim 1600$ K and is reflected as a second increment (though mild compared to the first) in the overall burning rate. At $T_s \leq 1200$ K, the surface reactions are slow so that the burning rate is primarily controlled by surface kinetic rates, while at $T_s \geq 2000$ K the surface reactions are very fast and diffusion becomes the rate controlling process. The predictions with mechanism B, however, show significantly lower burning rate for most of the surface temperature range considered. These predictions also fail to show the two-step increase seen with mechanism A.

The differences seen in burning rate predictions between the two mechanisms can be explained based on the relative contributions of the surface reactions to the overall mass burning rate. Figures 3 and 4 show the calculated surface reaction rates using mechanism A and B, respectively, for a uniform air stream at a strain rate $a=200 \text{ s}^{-1}$. For $T_s \leq 1600$ K, Fig. 3 shows that the dominant surface reaction is A5, while for $T_s \geq 1600$ K the reaction A4 becomes important. The carbon reactions with radical species are always found to be less than the reactions A4 and A5, but its contributions cannot be neglected for the surface temperature range 1400-1700 K. This is not the case with mechanism B. In this case, the reaction B2 ($C + O \rightarrow CO$) is the dominant reaction for $T_s \geq 1400$ K, while surprisingly the reaction B4 is the least important for the whole temperature range considered. In fact the reaction B4 is about two orders of magnitude smaller than A4. The surface reaction rates shown in Fig. 4 are, however, consistent with the results obtained with mechanism B by Bradley and co-workers [1] in their experimental and theoretical investigation on graphite particle oxidation (with mean diameter $\leq 4.3 \text{ }\mu\text{m}$) in a fuel lean methane-air flame (with post flame temperature below 1800 K). According to Ref. [23], the rate data for the reaction B5 strongly depend on the surface temperature and the particle size, and the present comparisons clearly indicate that they are not applicable for burning rate simulations of graphite rods having a diameter of 1 cm and surface temperatures ranging up to 2000 K.

The experiments of Makino et al. [3,5] have shown that two separate critical surface temperatures exist for the CO flame extinction and ignition. However, the numerical calculations employing mechanism A have failed to exhibit such extinction/ignition phenomena for a uniform air stream with a small amount of water vapor ($Y_{H_2O} = 0.005$), and at a strain rate of $a=200 \text{ s}^{-1}$ and temperature $T_\infty = 300$ K. Instead, a monotonic variation of the CO_2 mass fraction at the flame is observed and is shown in Fig. 5. Because of this smooth attachment/detachment of the flame to the graphite surface when the surface temperature is decreased/increased, the numerical integrations based on steady-state governing equations can proceed from a frozen state to a reacting state. However, when the composition of the oxidizer stream is replaced by oxygen stream (with $Y_{H_2O} = 0.005$) or the pressure of the air stream is increased to 0.79 MPa, the numerical calculations show the existence of a singularity or extinction/ignition phenomena as seen in Fig. 6 at $T_s = 1220$ K. These predicted trends are consistent with the observations made previously by Henriksen [7] in an analytical study employing a weakly burning CO flame regime. However, the flow conditions in the present analysis and that of Henriksen [7] are not exactly the same and more work is needed to verify these observations. On the other hand, if the experimental observations are accurate, then these preliminary results indicate that the semi-global mechanisms are incapable of predicting such extinction/ignition conditions and efforts must be made to include more realistic detailed reaction mechanisms for heterogeneous reactions.

Summary

Numerical simulations of graphite oxidation in a stagnation-point flow field are reported here. The application of semi-global mechanisms determined from previous experiments on oxidation of pyrolytic graphite particles are found to be incapable of predicting the mass burning rates of graphite rods. This clearly indicates the need to accurately characterize the transport effects at the surface and develop elementary reaction mechanisms to describe the graphite oxidation. Furthermore, the results on flame attachment/detachment indicate the need to carefully analyze flow conditions under which flame extinction/ignition will occur and the applicability of the currently available semi-global mechanisms to

such studies.

Acknowledgements

The author would like to thank A. Makino for helpful discussions.

References

- [1] Bradley, D., Dixon-Lewis, G., Habik, S.E., and Mushi, E.M.J., *Twentieth Symposium (International) on Combustion*, The Combustion Institute, p. 931 (1984).
- [2] Mitchell, R.E., *Twenty-second Symposium (International) on Combustion*, The Combustion Institute, p. 69 (1988).
- [3] Makino, A., Araki, N. and Mihara, Y., in preparation.
- [4] Adomeit, G., Hocks, W., and Henriksen, K., *Comb. Flame* **59**, p. 273 (1985).
- [5] Makino, A., and Law, C.K., *Comb. Sci. and Tech.* **73**, p.589 (1990).
- [6] Makino, A., *Comb. Flame* **81**, p. 166 (1990).
- [7] Matsui, K., and Tsuji, H., *Comb. Flame* **70**, p. 79 (1987).
- [8] Henriksen, K., *Twenty-third Symposium (International) on Combustion*, The Combustion Institute, p. 47 (1988).
- [9] Lau, C.W. and Niksa, S., *Comb. and Flame*, **90**, p.45 (1992).
- [10] Makino, A., *Comb. and Flame*, **90**, p.143 (1992).
- [11] Mitchell, R.E., Kee, R.J., Glarborg, P., and Coltrin, M.E., *Twenty-third Symposium (International) on Combustion*, The Combustion Institute, in press (1991).
- [12] Laurendeau, N.M., *Prog. Energy Comb. Sci.* **4**, p. 221 (1978).
- [13] Essenhigh, R.H., "Fundamentals of Coal Combustion," *Chemistry of Coal Utilization*, Second Supplementary Volume, M.A. Elliot (Ed.), Wiley, New York, p. 1153 (1981).
- [14] Howarth, J.B., *Twenty-third Symposium (International) on Combustion*, The Combustion Institute, p. 1107 (1990).
- [15] Chelliah, H.K. and Law, C.K., *ASME - Heat and Mass Transfer in Fires and Combustion Systems*, HTD-Vol 176, p. 49 (1991).
- [16] Smooke, M.D., Puri, I.K., and Seshadri, K., *Twenty-second Symposium (International) on Combustion*, The Combustion Institute, p. 1461 (1988).
- [17] Keyes, D.E. and Smooke, M.D., *J. Comp. Phys.* **73**, p. 267 (1987).
- [18] Miller, J.A., Kee, R.J., Smooke, M.D., and Grcar, J.F., Western States Section of the Combustion Institute, WSS/CI 84-10, April (1984).
- [19] Smooke, M.D., *J. Comp. Phys.* **48**, p.72 (1982).
- [20] Kee, R.J., Miller, J.A., and Jefferson, T.H., "Chemkin: A general purpose, problem-independent, transportable, fortran chemical kinetics code package," Sandia Report, SAND 80-8003.
- [21] Kee, R.J., Warnatz, J., and Miller, J.A., "A fortran computer code package for the evaluation of gas-phase viscosities, conductivities, and diffusion coefficients," Sandia Report, SAND 83-8209.
- [22] Yetter, R.A., Dryer, F.L., and Rabitz, H., *Comb. Sci. and Tech.*, in press (1991).
- [23] Turkdogan, E.T., Koump, V., Vinters, J.V. and Perzak, T.F., *Carbon*, **6**, p. 467 (1968).

Table 1A: Surface-reaction mechanism of Ref. [3], where, $\dot{s}_i = \nu_i W_i (\rho Y_i / W_i) A_i T^{\alpha_i} \exp(-E_i/RT)$.

Step	Reaction	A_i	α_i	E_i	Reference
A1	$C_s + OH \rightarrow CO + H$	1.65	0.5	0	[1]
A2	$C_s + O \rightarrow CO$	3.41	0.5	0	[1]
A3	$C_s + H_2O \rightarrow CO + H_2$	6.00×10^7	0.0	64300	[1]
A4	$C_s + CO_2 \rightarrow 2CO$	6.00×10^7	0.0	64300	[3]
A5	$2C_s + O_2 \rightarrow 2CO$	2.00×10^6	0.0	43000	[3]

Note: Units of \dot{s}_i , $A_i T^{\alpha_i}$, E_i , and T are in kg/m²/s, m/s, cal/mole, and Kelvin, respectively.

Table 1B: Surface-reaction mechanism of Ref. [1], with the rate \dot{s} expressed in terms of $k_i = B_i T^{\alpha_i} \exp(-E_i/RT)$ and partial pressure P_j .

Step	Reaction	i	B_i	n_i	E_i	\dot{s}_i
B1	$C_s + OH \rightarrow CO + H$	1	6.65×10^2	-0.5	0.0	$\dot{s}_1 = k_1 P_{OH}$
B2	$C_s + O \rightarrow CO$	2	3.61×10^2	-0.5	0.0	$\dot{s}_2 = k_2 P_O$
B3	$C_s + H_2O \rightarrow CO + H_2$	3	9.0×10^3	0.0	68100	$\dot{s}_3 = k_3 P_{H_2O}^{0.5}$
B4	$C_s + CO_2 \rightarrow 2CO$	4	4.8×10^5	0.0	68800	$\dot{s}_4 = k_4 P_{CO_2}^{0.5}$
B5	$C_s + (1/2)O_2 \rightarrow CO$	5	2.4×10^3	0.0	30000	$\dot{s}_5 = \left\{ \frac{k_5 P_{O_2} Y}{1 + k_6 P_{O_2}} \right\}^{-1}$
		6	2.13×10^1	0.0	-4100	$+ k_7 P_{O_2} (1 - Y)$
		7	5.35×10^{-1}	0.0	15200	where
		8	1.81×10^7	0.0	97000	$Y = \left[1 + \frac{k_8}{k_7 P_{O_2}} \right]^{-1}$

Note: Units of \dot{s}_i , E_i , P_j and T are in $\text{kg/m}^2/\text{s}$, cal/mole, atm., and Kelvin, respectively.

Table 2: The specific reaction-rate constants for the $CO/H_2O/O_2$ mechanism from Yetter et al. [22] in the form $k_j = B_j T^{\alpha_j} \exp(-E_j/RT)$.

Step	Reaction	B_j	α_j	E_j
1	$H + O_2 \rightleftharpoons OH + O$	1.91×10^{14}	0.0	16440
2	$H_2 + O \rightleftharpoons OH + H$	5.13×10^4	2.67	6290
3	$H_2 + OH \rightleftharpoons H_2O + H$	2.14×10^8	1.51	3430
4	$OH + OH \rightleftharpoons O + H_2O$	1.23×10^4	2.62	-1878
5	$H_2 + M \rightleftharpoons H + H + M^a$	4.57×10^{19}	-1.4	104380
6	$O + O + M \rightleftharpoons O_2 + M^a$	6.17×10^{15}	-0.5	0
7	$O + H + M \rightleftharpoons OH + M^a$	4.68×10^{18}	-1.0	0
8	$H + OH + M \rightleftharpoons H_2O + M^a$	2.24×10^{22}	-2.0	0
9	$H + O_2 + M \rightleftharpoons HO_2 + M^a$	6.76×10^{19}	-1.42	0
10	$HO_2 + H \rightleftharpoons H_2 + O_2$	6.61×10^{13}	0.0	2130
11	$HO_2 + H \rightleftharpoons OH + OH$	1.70×10^{14}	0.0	870
12	$HO_2 + O \rightleftharpoons OH + O_2$	1.74×10^{13}	0.0	-400
13	$HO_2 + OH \rightleftharpoons H_2O + O_2$	1.45×10^{16}	-1.0	0
14	$HO_2 + HO_2 \rightleftharpoons H_2O_2 + O_2$	3.02×10^{12}	0.0	1390
15	$H_2O_2 + M \rightleftharpoons OH + OH + M^a$	1.20×10^{17}	0.0	45500
16	$H_2O_2 + H \rightleftharpoons H_2O + OH$	1.00×10^{13}	0.0	3590
17	$H_2O_2 + H \rightleftharpoons H_2 + HO_2$	4.79×10^{13}	0.0	7950
18	$H_2O_2 + O \rightleftharpoons OH + HO_2$	9.55×10^6	2.0	3970
19	$H_2O_2 + OH \rightleftharpoons H_2O + HO_2$	7.08×10^{12}	0.0	1430
20	$CO + O + M \rightleftharpoons CO_2 + M^a$	2.51×10^{13}	0.0	-4540
21	$CO + OH \rightleftharpoons CO_2 + H$	1.50×10^7	1.3	-765
22	$CO + O_2 \rightleftharpoons CO_2 + O$	2.51×10^{12}	0.0	47690
23	$CO + HO_2 \rightleftharpoons CO_2 + OH$	6.03×10^{13}	0.0	22950
24	$HCO + M \rightleftharpoons CO + H + M^a$	1.86×10^{17}	-1.0	17000
25	$HCO + H \rightleftharpoons CO + H_2$	7.24×10^{13}	0.0	0
26	$HCO + O \rightleftharpoons CO + OH$	3.02×10^{13}	0.0	0
27	$HCO + OH \rightleftharpoons CO + H_2O$	3.02×10^{13}	0.0	0
28	$HCO + O_2 \rightleftharpoons CO + HO_2$	4.17×10^{13}	0.0	0

Note: Units are cal/mole, cm, and K.

^a The third body efficiencies are H_2 : 2.5, H_2O : 12.0, CO_2 : 3.8, CO : 1.9

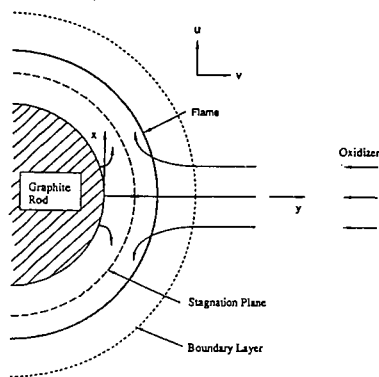


Figure 1: Illustration of the stagnation-point flow field near the graphite rod.

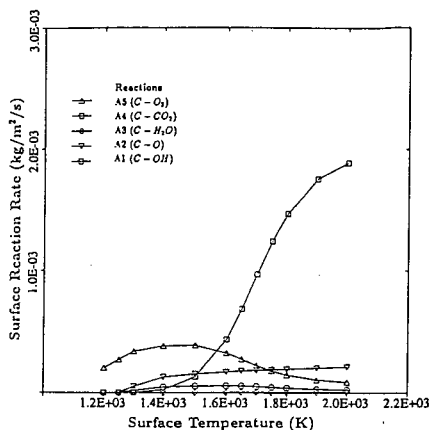


Figure 3: The surface reaction rates of mechanism A as a function of the surface temperature (T_s) in air (with $Y_{H_2O} = 0.005$) at a strain rate of $a = 200 \text{ s}^{-1}$.

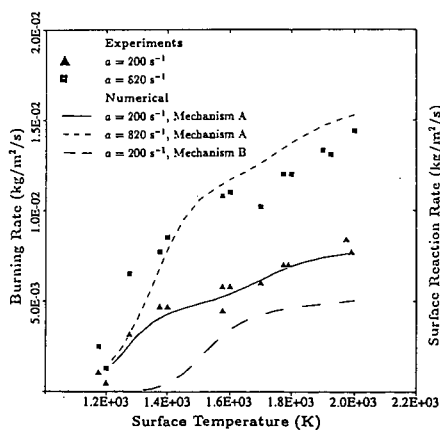


Figure 2: The burning rate of graphite as a function of the surface temperature (T_s) in air (with $Y_{H_2O} = 0.005$) from numerics and experiments of Makino et al. [3], for strain rates $a = 200$ and 820 s^{-1} .

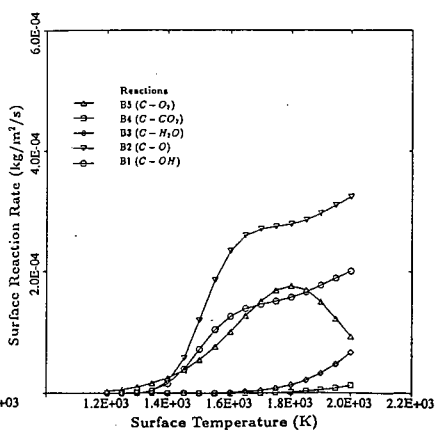


Figure 4: The surface reaction rates of mechanism B as a function of the surface temperature (T_s) in air (with $Y_{H_2O} = 0.005$) at a strain rate of $a = 200 \text{ s}^{-1}$.

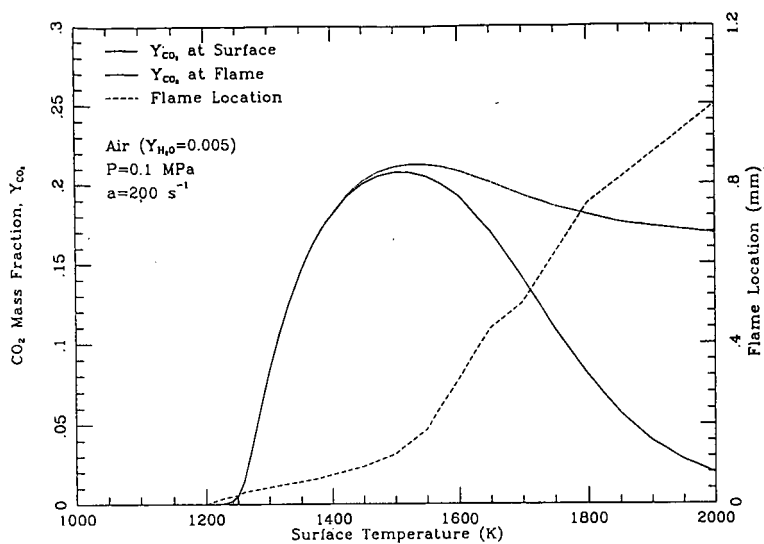


Figure 5: The variation of CO_2 mass fraction at the flame and at the surface, and the flame location as a function of the surface temperature for a air stream at $a = 200$ s $^{-1}$.

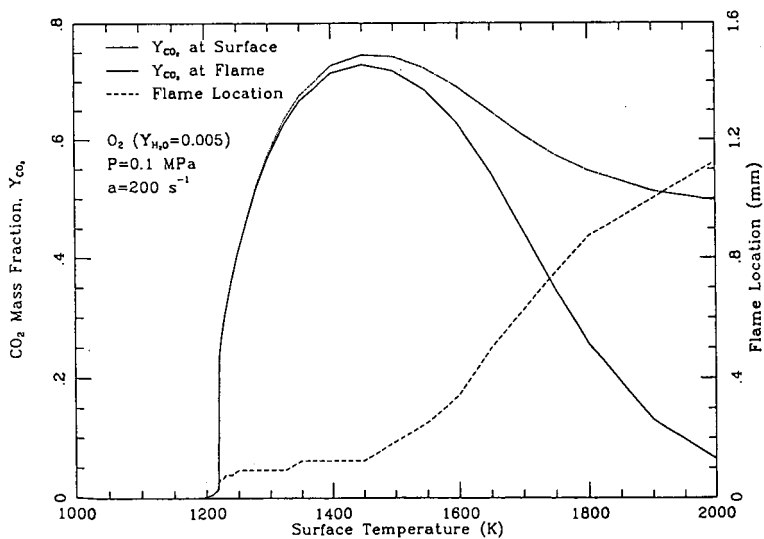


Figure 6: The variation of CO_2 mass fraction at the flame and at the surface, and the flame location as a function of the surface temperature for a oxygen stream at $a = 200$ s $^{-1}$.

MODELING OF COAL CONVERSION PROCESSES IN FIXED BEDS

M. Usman Ghani, Predrag T. Radulovic and L. Douglas Smoot
Advanced Combustion Engineering Research Center
Brigham Young University, Provo, Utah 84602

Keywords: Coal, Modeling, Fixed-beds.

Abstract

An advanced, one-dimensional fixed-bed coal gasification and combustion model is presented. The model considers separate gas and solid temperatures, axially variable solid and gas flow rates, variable bed void fraction, coal drying, devolatilization based on functional groups and depolymerization, vaporization and cross-linking, oxidation and gasification of char, and partial equilibrium in the gas phase. The model is described by 191 highly non-linear, coupled, first order differential equations. Due to the countercurrent nature of the gas and solids flow the system of equations constitutes a split-boundary value problem which is solved by converting it to an initial value problem. This paper presents a split back-and-forth shooting technique which exactly satisfies conditions at both the upper and the lower boundary and provides significant improvements in the predictions. Comparisons of the predicted and experimental results for an atmospheric, air-blown Wellman-Galusha gasifier fired with Jetson bituminous coal are presented.

Introduction

Combustion and gasification of coal in fixed beds or slowly moving beds is of great commercial interest as these systems can be integrated into combined cycle processes. In addition, these systems are reliable, require minimal pretreatment of feed coal, offer high thermal efficiencies, and generate easily disposable wastes. Due to these features, the fixed bed systems have been the focus of significant modeling efforts (Amundson and Arri, 1978; Yoon et al., 1978; Desai and Wen, 1978; Earl and Islam, 1985; Thorness and Kang, 1986; Bhattacharya et al., 1986). Most of these models make simplifying assumptions such as equal gas and solid temperatures, plug flow, constant bed porosity, instantaneous devolatilization and use oversimplified gas phase chemistry. More recently, Hobbs et al., (1992) presented a one-dimensional fixed-bed model, MBED-1, in which most of these assumptions were relaxed. A major contribution of their model was the integration of an advanced devolatilization submodel which is based on the functional group composition of the feed coal (Solomon and Hamblen, 1985). This model was combined with a semi-empirical correlation (Ko et al., 1988) for tar evolution. Their simulations showed that the predictions were very sensitive to the potential tar forming fraction of the coal and demonstrated a need for a more rigorous tar evolution submodel. In this paper, an improved model FBED-1 (Fixed-BED, 1-dimensional) is presented. In the FBED-1 model, devolatilization is based on a more rigorous Functional Group, Depolymerization, Vaporization, Crosslinking submodel (FG-DVC) proposed by Solomon et al., (1988). In the FG-DVC submodel, the DVC portion governs the tar evolution and is based on the chemical structure of the coal. In this paper, details relating to FBED-1 model are presented. For details regarding the FG-DVC submodel, the reader is referred to Solomon et al., (1988, 1990).

Conservation Equations

The core of the fixed-bed model, FBED-1, is a set of 191 coupled, first order ordinary differential equations. These equations simulate the chemical and physical processes taking place in both the gas and the solid phases during the coal conversion in a fixed-bed. The conservation equations for mass and energy form the foundation of the FBED-1 model. The gas and solid phase equations are coupled through the source terms. These source terms account for the release of mass from the solid phase to the gas phase, and energy exchange between the two phases. Tar is considered to be a pseudospecies in the FBED-1 formulation. The two-phase conservation equations have been derived by Crowe and Smoot (1979). The set of governing differential equations is listed in Table 1. It is also pointed out that the gas phase species continuity equations are solved only when the gas phase is assumed not to be in chemical equilibrium.

Auxiliary Equations

The set of auxiliary equations for FBED-1 is essentially the same as presented by Hobbs et al., (1992). Since plug flow is assumed for both the solid and the gas phases, the momentum equation is solved to calculate the gas phase pressure drop. Ergun's equation is used to calculate the friction factor and the bed void fraction is assumed to vary linearly between the feed coal and the product ash void fractions. At temperatures higher than a user-specified value, usually 1200 K, the gas phase is assumed to be in chemical and thermal equilibrium and its composition and temperature are computed by Gibbs free energy minimization. The option to keep tar either in or out of chemical equilibrium is provided in FBED-1. The calculation of heat and mass transfer coefficients and transport and thermodynamic properties of gas and tar phases are based on the same correlations as used and discussed by Hobbs et al., (1992).

Solution Methods

Due to the countercurrent flows of gas and solids, the system of governing equations constitutes a split boundary value problem. The input conditions for the solid phase are known at the top of the gasifier, whereas the input conditions for the gas phase are known at the bottom of the gasifier. This system of equations can be converted to an initial value problem and integrated from the top to the bottom of the gasifier, provided the initial estimates for the gas phase quantities are made available at the top of the gasifier. These estimates are made by a zero-dimensional, two-zone, well mixed, partial equilibrium submodel. The zero-dimensional submodel considers drying and devolatilization on one side and gasification and oxidation on the other to take place in separate zones. Its primary use is to provide initial estimates for the product gas enthalpy, composition and species flow rates, as well as the product tar composition and flow rate. Once these estimates are known, the system of equations is integrated from the top to the bottom of the gasifier using LSODE (Livermore Solver for Ordinary Differential Equations, Hindmarsh, 1983) package. Figure 1 shows the predicted results for an atmospheric, air-blown, dry-ash, Wellman-Galusha gasifier fired with Jetson bituminous coal. Experimental results (Thimsen et al., 1984) are also shown. Figure 1 also shows that the boundary conditions for the feed gas stream are not satisfied. The composition of product gas also does not compare well with the experimental data. It overpredicts the amount of H_2O and the product tar flow rate, and underpredicts the amount of O_2 in the feed gas stream, the wall heat loss and the feed gas temperature. Since the feed gas temperature was not reported, it was estimated to be 560 K to allow for the heat exchange between the ash and the feed gas below the gasifier bed. It is pointed out that the gas phase concentrations were determined assuming the gas phase to be in equilibrium in the zero-dimensional submodel. Only marginal improvements were observed in the product gas composition when the devolatilized gases were kept out of equilibrium in the drying and devolatilization zone. The predicted temperature and pressure profiles show the experimentally observed trends. These results clearly indicate a need for an improved solution method.

In order to improve on the FBED-1 predictions and to satisfy the boundary conditions for both the solid and the gas streams, a back-and-forth integration scheme has been developed and implemented. In this scheme, the differential equations are solved from the top to the bottom of the gasifier using the results of the two-zone, zero-dimensional submodel as the initial guess. After the first downward integration pass, the gas phase variables are initialized to the known input conditions. Then the gas phase equations are integrated from the bottom to the top of the gasifier. In the upward integration pass, the solid phase variables are held constant and the solid-gas exchange quantities are calculated from the values predicted during the downward integration pass. This yields a new guess for the gas phase quantities at the top of the gasifier which are then used for the next downward integration sweep. This improves the results and the next downward integration sweep, in which the complete set of equations is integrated, closely satisfies the feed gas boundary conditions except for the temperature. Finally, to satisfy the feed gas temperature, the split back-and-forth integration has been coupled with the shooting method with the product gas enthalpy as the iteration variable. In this scheme, the product gas enthalpy is varied, while all other gas phase quantities are held constant, and the complete set of equations is integrated from the top to the bottom of the gasifier. Once the feed gas temperature is converged within the specified tolerance, an upward pass is taken to compute the final product gas composition and temperature. Convergence is typically obtained in 8-10 iterations.

Figure 2 shows the results obtained using this revised solution method. The solution satisfies the feed gas composition and temperature. The product gas composition, the product tar flow rate and the wall heat loss also show marked improvement and compare well with the experimental data. The predicted pressure profile also compares well with the experimental data. The solid and the gas temperatures profiles show increase in the peak temperatures. This is caused by the higher amount of oxygen and lower amount of H₂O available which lead to higher oxidation rate and thus higher temperatures. The predicted solid temperature profile exceeds the peak measured temperature but compares reasonably well with the experimental data. Finally, the product gas temperature still does not compare well with the experimental data. It should be noted that the reported effluent gas temperature is at the gas-off take location whereas the predicted product gas temperatures is at the gasifier bed top. A proper submodel to account for the heat transfer in the free board zone will improve these predictions.

Acknowledgement

This work was sponsored by the U. S. Department of Energy, Morgantown Energy Technology Center (Contract No. DE-AC21-86MC23075) under subcontract from Advanced Fuel Research, Inc., East Hartford, CT.

References

- Amundson, N. R. and Arri, L. E., "Char Gasification in a Countercurrent Reactor," AIChE J., **24**, 87 (1978).
- Bhattacharya, A., Salam, L., Dudukovic, M. P. and Joseph, B., "Experimental and Modelling Studies in Fixed-Bed Char Gasification," Ind. Eng. Chem. Process Des. Dev., **25**, 988 (1986).
- Crowe, C. T. and Smoot, L. D., "Multicomponent Conservation Equations," in Pulverized-Coal Combustion and Gasification, Smoot, L. D. and Pratt, D. T., editors, Plenum Press, New York (1979).
- Desai, P. R. and Wen, C. Y., "Computer Modeling of the MERC Fixed Bed Gasifier," MERC/CR-78/3, U. S. Department of Energy, Morgantown, West Virginia (1978).
- Earl, W. B. and Islam, K. A., "Steady-state Model of a Lurgi-type Coal Gasifier," Innovation in the Process and Resource Industry CHEMCA 85, Proceedings of the Thirteenth Australian Chemical Engineering Conference, Perth, Australia, paper c2b, 289 (1985).
- Hindmarsh, A. C.: "ODEPACK, A Systematized Collection of ODE Solvers," in Scientific Computing (R. S. Stepleman, editor), Vol. 1. p. 55, IMACS Transactions on Scientific Computation, North-Holland, Amsterdam (1983).
- Hobbs, M. L., Radulovic, P. T., and Smoot, L. D., "Modeling Fixed-Bed Coal Gasifiers," AIChE J., **38**, 681 (1992).
- Ko, G. H., Sanchez, D. M., Peters, W. A. and Howard, J. B., "Correlations for Effects of Coal Type and Pressure on Tar Yields from Rapid Devolatilization," 22nd Symposium (International) on Combustion, The Combustion Institute, Pittsburgh, Pennsylvania, 115 (1988).
- Radulovic, P. T., Smoot, L. D., Ghani, M. U., Hobbs, M. L., and Yi, S., "Comprehensive Fixed-Bed Modeling, Review, Development, Evaluation and Implementation," in Measurement and Modeling of Advanced Coal Conversion Processes, Solomon, P. R., Hamblen, D. G., Serio, M. A., Smoot, L. D., and Brewster, B. S., Final Report for the U.S. Department of Energy, Morgantown Energy Technology Center, Morgantown, WV, Advanced Fuel Research, Inc. East Hartford, CT, Brigham Young University, Provo, UT, Contract No. DE-AC21-86MC23075 (1992).
- Solomon, P. R. and Hamblen, D. G., "Pyrolysis," in Chemistry of Coal Conversion, ed. Schlosberg, R. H., Plenum Press, New York (1985).
- Solomon, P. R., Hamblen, D. G., Carangelo, R. M., Serio, M. A. and Deshpande, G. Y., "General Model of Coal Devolatilization," Energy and Fuels, **2**, 405 (1988).
- Solomon, P. R., Hamblen, D. G., Yu, Z. Z. and Serio, M. A., "Network Models of Coal Thermal Decomposition," Fuel, **69**, 754 (1990).
- Thimsen, D., Maurer, R. E., Pooler, A. R., Pui, D. Y. H., Liu, B. Y. H. and Kittelson, D. B., "Fixed-Bed Gasification Research using U.S. Coals," **2**, U.S. Bureau of Mines Contract H0222001, (1984).

Thorsness, C. B. and Kang, S. W., "A General-Purpose, Packed-Bed Model for Analysis of Underground Coal Gasification Processes," UCID-20731, Lawrence Livermore National Laboratory, University of California, Livermore, California (1986).

Yoon, H., Wei, J. and Denn, M. M., "A Model for Moving-bed Coal Gasification Reactors," *AIChE J.* 24, 885 (1978).

Nomenclature

Symbol Definition and Units

<i>A</i>	Cross sectional area of reactor, m^2
<i>D</i>	Diffusivity, m^2/s
<i>h</i>	Enthalpy, J/kg
<i>Q</i>	Heat loss, <i>watts</i>
<i>r</i>	Volumetric reaction rate, $kg/m^3 s$
<i>W</i>	Mass flow rate, kg/s
<i>z</i>	Axial distance, <i>m</i>

Subscripts Definition

<i>d</i>	Devolatilization
<i>g</i>	Gas
<i>gw</i>	Gas-to-wall
<i>i</i>	Index for drying, devolatilization, gasification and oxidation reactions
<i>j</i>	Index for elements C, H, O, N, and S
<i>l</i>	Index for gaseous species
<i>moisture</i>	Moisture
<i>sg</i>	Solid-to-gas
<i>sw</i>	Solid-to-wall

Superscripts Definition

<i>gas</i>	Gas
<i>tar</i>	Tar

Table 1. Governing Equations for FBED-1

Overall Gas Continuity	$\frac{dW_g}{dz} = A \sum_{i=1}^6 r_i$	(1)
Overall Solid Continuity	$\frac{dW_s}{dz} = -A \sum_{i=1}^6 r_i$	(2)
Gas Phase Energy	$\frac{dW_g h_g}{dz} = A(Q_{rg} - Q_{rw} + \sum_{i=1}^6 r_i h_{ig})$	(3)
Solid Phase Energy	$\frac{dW_s h_s}{dz} = A(-Q_{rg} - Q_{rw} - \sum_{i=1}^6 r_i h_{is})$	(4)
Gas Phase Species Continuity	$\frac{dW_{g,i}}{dz} = A \sum_{j=1}^6 r_{i,j}^{gas}$	(5-26)
Gas Phase Elemental Continuity	$\frac{dW_{g,j}}{dz} = A \sum_{i=1}^6 r_{i,j}$	(27-31)
Overall Tar Continuity	$\frac{dW_{tar}}{dz} = A r_d^{tar}$	(32)
Tar Elemental Continuity	$\frac{dW_{tar,j}}{dz} = A r_{d,j}^{tar}$	(33-37)
Moisture Continuity	$\frac{dW_{moisture}}{dz} = -A r_{drying}$	(38)

Notes:

1. Equations 39-164 describe the FG-DVC devolatilization submodel (Radulovic et al., 1992).
2. Equations 165-191 describe the lower bound of the distribution function for the gas phase tar cracking reactions and follow the FG-DVC formulation (Radulovic et al., 1992).
3. Equations 5-26 are solved only when the gas phase is not considered to be in chemical equilibrium.
4. $i=1-6$ represents drying, devolatilization, CO_2 , H_2 , H_2O gasification and oxidation reactions respectively.
5. $j=1-5$ represents elements C, H, O, N, and S respectively.
6. $j=1-22$ represents 22 gaseous species considered in FBED-1.

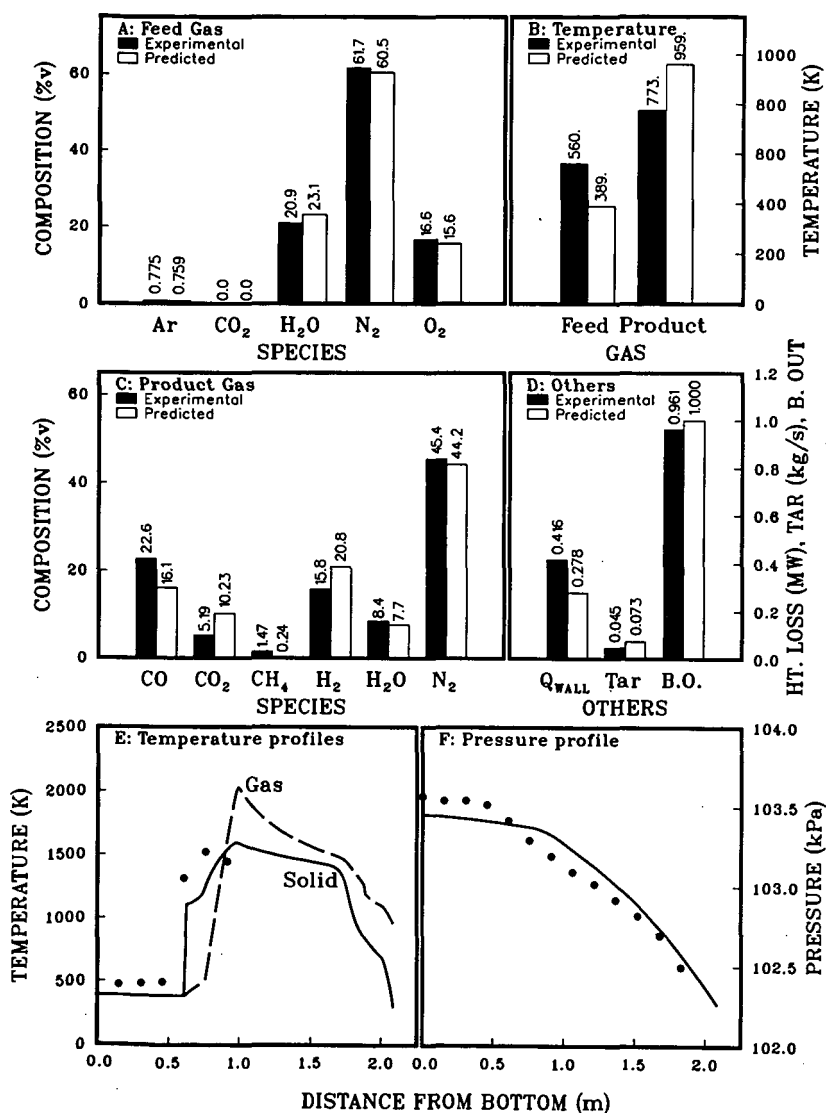


Figure 1. Comparison of predicted and experimental results for an atmospheric, air-blown, dry-ash, Wellman-Galusha gasifier fired with Jetson bituminous coal. The predictions are obtained by converting the system of equations to an initial value problem.

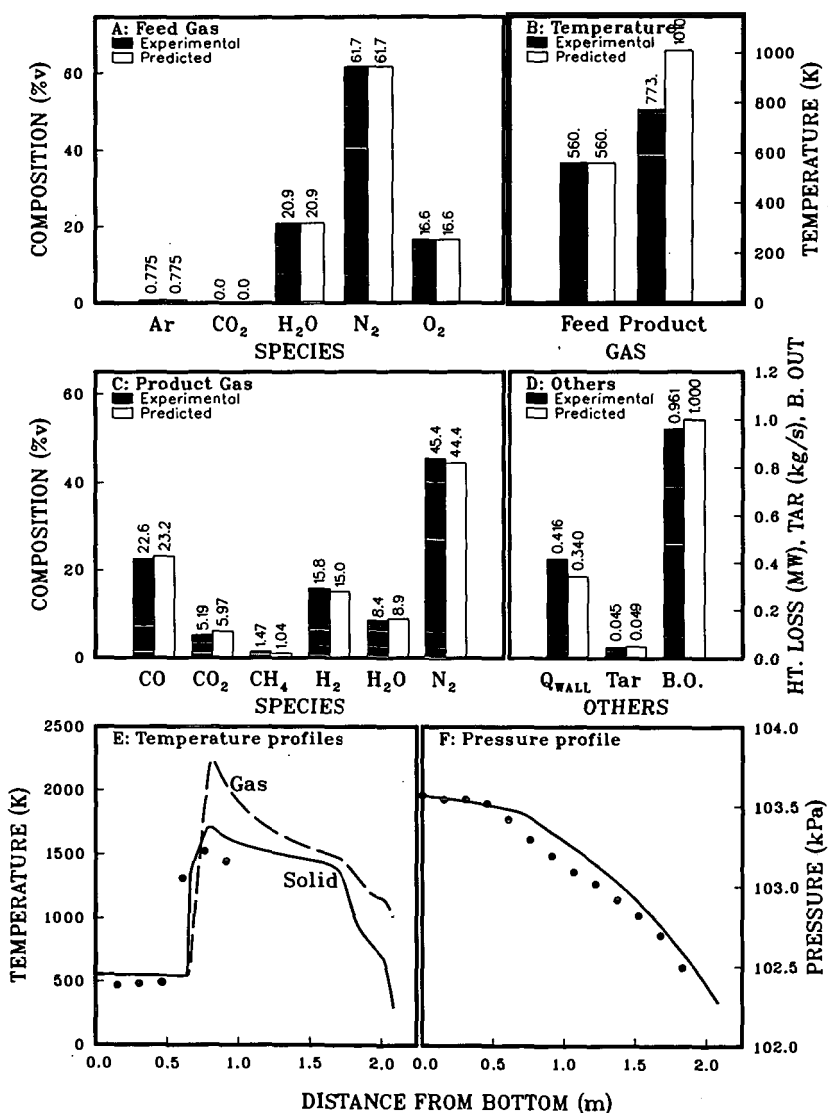


Figure 2. Comparison of predicted and experimental results for an atmospheric, air-blown, dry-ash, Wellman-Galusha gasifier fired with Jetson bituminous coal. The predictions are by a split back-and-forth shooting method.

NUMERICAL SIMULATION OF PULVERIZED COAL COMBUSTION AND EMISSION

C.F. Bender, R.H. Essenhigh¹, U. Ghia², and M.L. Mittal
Program for Computational Reactive Mechanics
Ohio Supercomputer Center, Columbus, OH 43212

Keywords: Turbulence, Particle Mixing, Fluid Flow for Combustion

1 Introduction

The development of accurate computer simulation tools for coal combustion and emission represents a complex task. Like combustion of other fuels, coal combustion has the coupling of: i) exothermic chemical reactions; ii) heat transfer; and iii) two phase fluid flow, but with added complexities due to particle pyrolysis, the internal burning of the particles, and formation of ash and slag. At present, there are a number of commercial codes (proprietary in nature) that have been developed and/or are in use for aid in boiler design and performance predictions. There are many programs in the academic institutions as well, like the programs at the University of Illinois, Imperial College of London, the University of New Castle in Australia etc. The program at the Brigham Young University (BYU) has been the most successful. Many industries use this code. This program uses time averaged equations for fluid flow and 'engineering' rate equations for combustion and is suitable for use even on workstations. Essenhigh's group at The Ohio State University has developed a one-dimensional model of a coal flame to study the kinetics of coal combustion with focus on the reactivity aspects.

The proposed program at the Ohio Supercomputer Center is complementary to the BYU program. We propose to use high performance computing techniques for numerical simulation of pulverized coal combustion and emission with details of fluid mechanics, heat transfer, and reaction kinetics for combustion. The BYU program can give the directions and help to validate some of our results. Under this program, we also propose to make a comparative performance evaluation of different models/combination of models for pyrolysis, volatile combustion, and char oxidation. Unlike in other programs, we have started with the simulation of two phase fluid flow to study the turbulent mixing of the coal particles and the effect of particles on the flow.

Turbulent mixing of particles has been studied by many authors [Crowe et al. (1988)]. The majority of the reviewed studies have used flow models involving either the time-averaged properties of the turbulence, or have treated the turbulent flow as a random field. However, with the recent developments in the understanding of turbulent shear flows, it is being suggested that particle dispersion in free shear layers might be strongly dependent on the time scale of the large organized structures in the flow. Samimy and Lele (1990) have recently studied the particle motion in a temporally evolving compressible shear layer. All of these studies emphasize particle dispersion by an idealized fluid in simple geometries and do not account for viscosity and the effects of combustor geometry.

The purpose of the present study is to simulate the particle dispersion in a temporally and spatially evolving turbulent shear layer. To the best knowledge of the authors, this is the first study in which a direct numerical simulation of particle dispersion by a viscous turbulent flow field for a combustor type geometry is carried out. It is known that the presence of large number of

¹The Ohio State University, Columbus, Ohio

²University of Cincinnati, Cincinnati, Ohio.

solid particles or liquid droplets in the turbulent flow modifies the turbulent structure [Elghobasi and Abou-Arab (1983)]. The present study will determine the flow conditions in the combustor as modified by the presence of large number of coal particles.

2 Mathematical modeling

The combustion chamber is represented as an axisymmetric sudden step-expansion geometry. An inert gas flow with swirl is considered. Particles of three different sizes are injected at three different radial and four different angular positions in the throat region. As the gas flows, the particles are dispersed in the combustion chamber by turbulence. Because of the large number of actual coal particles in the combustor region, the representation is confined to a statistical sample. Therefore, each of these sample particles characterize a 'parcel' of like numbers all having the same initial size, velocity, and temperature. In the present analysis, radiation is not included in the energy equation.

2.1 The gaseous phase

The fluid flow in the combustion chamber is represented mathematically by the time-dependent Navier-Stokes, equations expressed as a transport equation for the vorticity vector ω .

$$\frac{\partial \omega}{\partial t} + (\mathbf{V} \cdot \nabla) \omega = (\omega \cdot \nabla) \mathbf{V} - \frac{1}{Re} (\nabla \times \nabla \times \omega) - \nabla \times \mathbf{S}_p \quad (1)$$

where

$$\nabla \times \mathbf{V} = \omega \quad (2)$$

and \mathbf{S}_p is the interfacial drag force resulting from the interaction between particles and medium.

The incompressibility constraint

$$\nabla \cdot \mathbf{V} = 0. \quad (3)$$

for the present case of axisymmetric flow involving only two spatial coordinates, defines a stream function ψ given by

$$\mathbf{V} = \nabla \psi \times \hat{e}_3 \quad (4)$$

where \hat{e}_3 is a unit vector parallel to x^3 . The governing equation for ψ is then obtained using Eq.(2).

The energy equation in conservation form with S_T as the source term can be written as

$$\frac{\partial T}{\partial t} + \nabla \cdot (\mathbf{V} T) = \frac{1}{Pe} [\nabla \cdot (\kappa \nabla T)] + S_T \quad (5)$$

2.2 Particulate phase

Lagrangian equations are used to compute the motion and heating of each sample as it traverses the gas in the combustion chamber. The usual assumptions are employed to derive these equations. Assuming non-deformable spherical particles, with density much higher than that of the fluid, virtual mass force, pressure gradient force and Basset force are all neglected. Particle-particle interaction and other force fields such as gravity are also presently not included in the analysis. The governing equations for the particle in nondimensional form are written as:

$$\frac{d\mathbf{V}_p}{dt} = \frac{1 + 0.15 Re_p^{2/3}}{\gamma_r} (\mathbf{V}_f - \mathbf{V}_p) \quad (6)$$

where $Re_p = |\mathbf{V}_f - \mathbf{V}_p| \gamma_d Re$ and $\gamma_r = \tau_p / \tau_f = \gamma_p \gamma_d^2 (Re/18)$, the ratio of the aerodynamic response time and the time scale for large turbulent structures. Thus, γ_d characterizes the effectiveness of the large-scale structures for particles moving laterally in the mixing region. Further, $\gamma_p = \rho_p / \rho_f$ and $\gamma_d = d_p / d$. Here, d denotes diameter, and subscripts p and f designate particle and fluid, respectively.

The particle energy equation is given as:

$$\frac{m_p dh_p}{dt} + r_p(h_p - h_f) = \dot{Q} \quad (7)$$

The parameter \dot{Q} is the gain or loss by convection or radiation with the gas phase.

Eqs. (1) and (6) are coupled through the term S_p given by

$$S_p = \sum_n \frac{(1 + 0.15 Re_p^{2/3}) \rho_p}{\gamma_p \gamma_d^2 (Re/18) \rho_f} \alpha^n (\mathbf{V}_f - \mathbf{V}_p) \quad (8)$$

with $\alpha^n = \frac{N \pi d_p^3}{6 \Delta v}$, N being the number of particles represented by the trajectory n and Δv is the computational cell volume.

2.3 Solution procedure

The analysis as well as the numerical solution procedure used to simulate the fluid flow follow the work of Osswald, et al. (1984). Writing the vorticity vector as

$$\boldsymbol{\omega} = \omega^1(r, z) \bar{e}_1 + \omega^2(r, z) \bar{e}_2 + \omega^3(r, z) \bar{e}_3 \quad (9)$$

where ω^i are the contravariant components of vorticity and \bar{e}_i are the covariant base vectors parallel to ξ^i coordinates, the governing equation for ω^3 in a generalized orthogonal curvilinear coordinate system (ξ^1, ξ^2, ξ^3) is derived.

$$\begin{aligned} & \sqrt{g} \frac{\partial \omega^3}{\partial t} + \frac{\partial}{\partial \xi^1} \left(\omega^3 \frac{\partial \psi}{\partial \xi^2} \right) - \frac{\partial}{\partial \xi^2} \left(\omega^3 \frac{\partial \psi}{\partial \xi^1} \right) \\ &= \frac{1}{Re} \left[\frac{\partial}{\partial \xi^1} \left(\frac{g_{22}}{\sqrt{g}} \frac{\partial}{\partial \xi^1} (g_{33} \omega^3) \right) + \frac{\partial}{\partial \xi^2} \left(\frac{g_{11}}{\sqrt{g}} \frac{\partial}{\partial \xi^2} (g_{33} \omega^3) \right) \right] \end{aligned} \quad (10)$$

g_{ii} are defined as

$$g_{ii} = \sum_{k=1}^3 \left(\frac{\partial x^k}{\partial \xi^i} \right) \left(\frac{\partial x^k}{\partial \xi^i} \right) \quad (11)$$

with $g = g_{11} g_{22} g_{33}$ and $h_i = \sqrt{g_{ii}}$.

The stream function ψ is determined from

$$\frac{\partial}{\partial \xi^1} \left(\frac{g_{22}}{\sqrt{g}} \frac{\partial \psi}{\partial \xi^1} \right) + \frac{\partial}{\partial \xi^2} \left(\frac{g_{11}}{\sqrt{g}} \frac{\partial \psi}{\partial \xi^2} \right) = -\sqrt{g} \omega^3. \quad (12)$$

The azimuthal component of velocity v_ϕ gives the swirl velocity of the flow. The governing equation for v_ϕ is

$$\begin{aligned} & \frac{\partial v_\phi}{\partial t} + \frac{1}{\sqrt{g}} \left[\frac{\partial}{\partial \xi^1} \left(\frac{\partial \psi}{\partial \xi^2} v_\phi \right) - \frac{\partial}{\partial \xi^2} \left(\frac{\partial \psi}{\partial \xi^1} v_\phi \right) \right] + \frac{v_x v_\phi}{h_1 h_3} \frac{\partial h_3}{\partial \xi^1} + \frac{v_r v_\phi}{h_2 h_3} \frac{\partial h_3}{\partial \xi^2} = \\ & + \frac{1}{Re} \times \frac{1}{\sqrt{g}} \left[\frac{\partial}{\partial \xi^1} \sqrt{\frac{g_{22}}{g_{11} g_{33}}} \frac{\partial}{\partial \xi^1} \left(\frac{v_\phi}{\sqrt{g_{33}}} \right) + \frac{\partial}{\partial \xi^2} \sqrt{\frac{g_{11}}{g_{22} g_{33}}} \frac{\partial}{\partial \xi^2} \left(\frac{v_\phi}{\sqrt{g_{33}}} \right) \right] \\ & + \frac{1}{Re} \left[\frac{1}{g_{11}} \frac{\partial \sqrt{g_{33}}}{\partial \xi^1} \frac{\partial}{\partial \xi^1} \left(\frac{v_\phi}{\sqrt{g_{33}}} \right) + \frac{1}{g_{22}} \frac{\partial \sqrt{g_{33}}}{\partial \xi^2} \frac{\partial}{\partial \xi^2} \left(\frac{v_\phi}{\sqrt{g_{33}}} \right) \right] - \frac{1}{\sqrt{g_{33}}} \frac{\partial p}{\partial \xi^3} \end{aligned} \quad (13)$$

In the generalized orthogonal coordinate system, the energy equation (5) transforms as

$$\begin{aligned} & \sqrt{g} \frac{\partial T}{\partial t} + \frac{\partial}{\partial \xi^1} \left(T \frac{\partial \psi}{\partial \xi^2} \right) - \frac{\partial}{\partial \xi^2} \left(T \frac{\partial \psi}{\partial \xi^1} \right) \\ & = \frac{1}{Pe} \left[\frac{\partial}{\partial \xi^1} \left(\frac{\sqrt{g}}{g_{11}} \frac{\partial}{\partial \xi^1} (\kappa T) \right) + \frac{\partial}{\partial \xi^2} \left(\frac{\sqrt{g}}{g_{22}} \frac{\partial}{\partial \xi^2} (\kappa T) \right) \right] + S_T \sqrt{g} \end{aligned} \quad (14)$$

2.3.1 Boundary and initial conditions

At the radial boundaries, the flow conditions are derived from symmetry across the centerline and zero slip at the walls. The streamwise asymptotic forms of the governing equations (10-14) are solved to provide the inflow/outflow boundary conditions; this approach maintains consistency between the boundary values and the interior solution. The initial conditions correspond to a flow starting impulsively from rest.

2.3.2 Numerical mesh

An appropriate coordinate system is obtained by a conformal mapping of the sudden-expansion geometry to a uniform cross-section configuration. This mapping is further augmented by clustering/stretching transformations so as to provide resolution of the prevailing flow features and to provide for placing the inflow and outflow boundaries at upstream and downstream infinity, respectively.

2.3.3 Numerical solution

Starting from the initial state, the vorticity field is advanced using an alternating-direction implicit method. The corresponding stream-function distribution is obtained by a direct, fully implicit solution of the elliptic stream function equation. The time evolution of the flow field is pursued as long as desired. All spatial derivatives are discretized using second-order accurate central differences. Care is taken to ensure proper grid-point placement so as to obtain satisfactory results.

3 Results and discussion

The numerical computations have been performed at the Ohio Supercomputer Center using the CRAY Y-MP 8/864 supercomputer. Figure 1 shows the geometry and the grid distribution for the sudden axisymmetric step-expansion geometry. A grid of 635 points is used in the axial direction and 132 points in the radial direction, with $Re = 1.0 \times 10^3$ and time step $\Delta t = 2.0 \times 10^{-6}$. Three

values of γ_d , namely $\gamma_d = 10.0^{-5}$, 20.0^{-5} , and 40.0^{-5} are considered to simulate the effect of particle size on mixing. Figures 2-4 show the instantaneous particle positions and vorticity contour lines at nondimensional time $t = 0.695$, 0.815 , and 0.820 . Only regions containing particles are shown. Initially, the entering particles move downstream in a rectilinear fashion with the fluid but then the fluid vorticity starts to affect their movement. The lighter particles start circulating first, with all particles eventually following suit. At later times, a rather interesting feature develops. As seen from their distribution overlaid on the vorticity field, the particles tend to be entrapped by the evolving large-scale vortex structure. This feature appears to be initiated in regions of reduced axial fluid velocity. At a later time, some of these particles move upstream while others move downstream at the upper periphery of the middle vortex structure; those in the region between two vortex structures move very rapidly towards the lower periphery of the downstream vortex.

The curves for temperature distribution are not shown here. The fluid temperature gives the thermal environment for the particles.

4 Conclusion

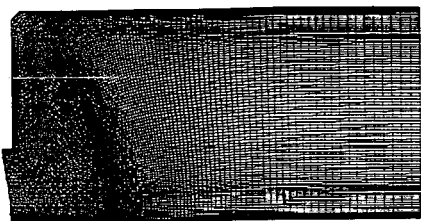
The numerical simulation of coal combustion is a challenging computational problem as it covers many different phenomena. The present effort represents a first step to provide a unified approach to the problem, using direct numerical simulation. This simulation has considered particle mixing in an adiabatic isothermal flow.

5 Future work

Work is in progress to study the combustion of single coal particle. This study needs the solution of the energy equation with radiation and the solution of the energy equation for particulate phase. Simultaneously, we are making parametric studies to determine the effect of swirl on particle dispersion and the effect of particle motion on the fluid flow.

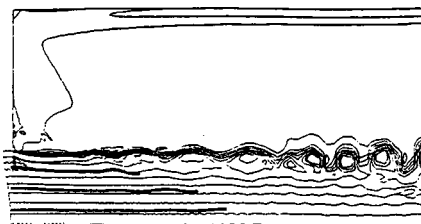
References

- [1] G. A. Osswald, K. N. Ghia, and U. Ghia, *AIAA Paper* 84-1584 (1984)
- [2] J. N. Chung and T. R. Troutt, *J. Fluid. Mech.* 186, 199-222 (1988)
- [3] M. Samimy and S. K. Lele, *Phys. Fluids* (1990) To appear
- [4] V.G. McDonnell and G. S. Samuelsen, *AIAA Paper* AIAA-91-0082 (1991)
- [5] S.E. Elghobashi and T. W. Abou-Arab, *Phys. Fluids* 26, 931-938 (1983)



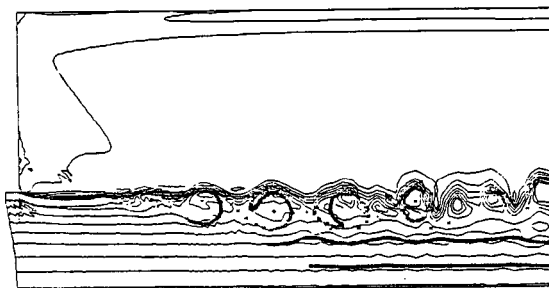
Typical Grid 635 x 132

Figure 1.



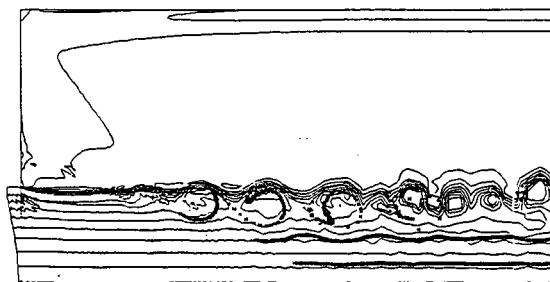
$x=0.01$, $Re=1000$, $Time=0.625$, $\xi=2.06$

Figure 2.



$x=-0.31$, $Re=1000$, $Time=0.820$, $\xi=2.06$

Figure 3.



$x=0.01$, $Re=1000$, $Time=0.815$, $\xi=2.06$

Figure 4.

APPLICATION OF THE STOCHASTIC MODEL OF PARTICLE TURBULENT DISPERSION IN THE MODELING AND DESIGN OF A HIGH EFFICIENCY COAL COMBUSTOR

Yuxin Zhao, David S. Pines, Peter R. Solomon, Michael A. Serio
Advanced Fuel Research, Inc
87 Church Street, East Hartford, CT 06108

Key words: turbulence, particle dispersion, combustion modeling.

Introduction

In the modeling of pulverized coal combustion, the particle dispersion and transport in a turbulent flow are important issues. The accurate predictions of the flame structure and the radiation distribution rely strongly on how precisely the particle dispersion can be modeled. During the past decade, two major types of models have been developed: empirical and stochastic. In the empirical models by Lockwood et al. [1] and Smith et al. [2], the dispersion is assumed to be a diffusion process and is modeled by adding a diffusion velocity component to the mean particle velocity determined from the mean gas velocity. Empirical relations are used to calculate the diffusion velocity from the gas turbulence [1,2]. On the other hand, the stochastic models [3-5] treat particle motions in turbulence statistically. They trace the instantaneous interactions between particles and the turbulent eddies. Since the gas turbulence is stochastic in nature, these models are favored.

We have employed a stochastic model of particle dispersion in modeling a coal combustor for the design of a high temperature recuperative gas turbine topping cycle system [6]. The combustor contains a Radiatively Enhanced, Aerodynamically Cleaned Heat-Exchanger (REACH-Exchanger). The combustor is configured so that the working fluid is heated by the radiation from the coal flame while clean combustion gases are used to shield the ceramic heat exchanger tubes from the corrosive coal and ash particles. One of the important issues is to find the effect of various firing schemes on the particle dispersion, in order to prevent the ash particles from fouling the surface of the ceramic tubes.

In this paper, we present the further modification of the stochastic model and a few case studies showing how the firing scheme affects the particle dispersion. The combustion process is modeled by a 2D finite difference combustion code PCGC-2 [7].

Stochastic Model

The particle motion is described in a Lagrangian framework as

$$\begin{cases} \frac{dU_i}{dt} = \Gamma(\bar{V}_i - U_i) + \Gamma V'_i + g_i \\ \frac{dX_i}{dt} = U_i \end{cases} \quad (1)$$

where U_i and V_i are the i^{th} ($i=1,2,3$) components of velocity vectors of a particle and the gas, respectively; Γ accounts for the Stokes drag; X is the spatial coordinate of the particle; g_i is the gravity. Stochastic processes are specified with upper case characters and their realizations are given with

corresponding lower case characters. A prime indicates the fluctuation component of a stochastic process, and a bar indicates the mean value. In the stochastic model, V_i' is simulated with a random number generator. The particle is assumed to interact with eddies when it travels along with the gas stream. The gas velocity is assumed to be constant in each eddy. The length of the eddy is given by the length scale of the turbulence and the eddy decays with time according to the time scale. In other words, a particle sees a new eddy when it enters another eddy or the old one fades away. In the previous work [3,4,5], V_i' was generated directly by Monte Carlo methods and the interaction is handled in the numerical integration. A disadvantage of this method is that the results can be largely influenced by the numerical time step and it is not very efficient since the stochastic spectrum of the turbulence is not used. In this study, improvements of these early models were made based on the recent developments in the numerical integration of stochastic differential equations [8,9].

The stochastic characteristics of V_i are given by those of V_i' (turbulence model, k-ε) in terms of k , l_0 , and t_0 , where k is the turbulence kinetic energy, and l_0 and t_0 are the length and time scales of the turbulence. V_i' is a stochastic process of both time, t , and distance, x . The autocorrelation functions of t and x are by definition

$$R_{V_i'}(\Delta t) = \exp(-|\Delta t|/t_0) \quad (2)$$

and

$$R_{V_i'}(\Delta x) = \exp(-|\Delta x|/l_0) \quad (3)$$

The double correlation is not readily available and is assumed to be

$$R_{V_i'}(\Delta x, \Delta t) = \exp(-\sqrt{(\Delta t/t_0)^2 + (\Delta x/l_0)^2}) \quad (4)$$

Since a particle sees the gas when it travels, the decay of the gas velocity seen by a particle traveling with velocity U is a function of Δt only. If $R_{V_i'}$ decays quickly enough against x , we have

$$R_{V_i',p}(\Delta t) = \exp(-\beta|\Delta t|) \quad (5)$$

where

$$\beta = \sqrt{(1/t_0)^2 + ((\bar{U}(x,t) - \bar{V}(x,t))/l_0)^2} \quad (6)$$

The second subscript p of R means that the correlation in Eq. (5) is for the gas seen by particles. From Eq. (5), we know that when seen by particles, the gas velocity fluctuation, V_i' , can be approximated with an Ornstein-Uhlenbeck process and can be generated with a filtered white noise[8]

$$\frac{dV_i'}{dt} = -\beta V_i' + \sigma_v \sqrt{2\beta} \xi_i(t) \quad (7)$$

where $\sigma_v = (2/3k)^{0.5}$. $\xi_i(t)$ is a Gaussian white noise function. Or more formally

$$dV_i' = -\beta V_i' dt + \sigma_v \sqrt{2\beta} dW_i(t) \quad (8)$$

where $dW_i(t)$ is an incremental Wiener process of Gaussian, $N(0, \Delta t)$. Since Eq. (8) contains explicitly σ_v and β , it can generate V_i' with correct gas turbulence statistics. We used differential equations (1) and (8) to model the particle dispersion by turbulence.

This set of equations is, however, intrinsically stiff for coal combustion problems, since very often the time scale, $1/\beta$, is much smaller than the particle relaxation time scale $1/\Gamma$. An implicit Euler scheme was employed in the integration to maintain the numerical stability.

Case Studies

To investigate the effect of firing schemes on the coal particle dispersion, combustion in the REACH Reactor was modeled using various firing schemes. We present here only two of the cases studied. Table 1 lists the conditions of these two cases. The reactor is a 9 meter tall cylinder which is 2.8 meters in diameter. Coal particles were fired with the primary air at the center top position. Gas streams were injected from a number of annulus inlets. A schematic diagram of this reactor is given in Figure 1. The top view shows the relative positions of the inlets. The ceramic heat exchange tubes are located around the flame and next to the refractory wall, but they were not included in the calculations. The same mass flux of coal particles and air were used for both cases, except that there was a tertiary CH_4 /air stream in Case 2. The diameter of the secondary air conduit in Case 1 was 1.27 meters, which was slightly larger than the 1.0 meters given in Figure 1 for Case 2.

The combustion was modeled with PCGC-2 [7] which provided the gas velocity and turbulence field information. The particle stochastic differential equations (1) and (8) were then solved. In each calculation, 100 particles were injected from 5 positions inside the primary tube and 100 particle trajectories were generated with our stochastic model. We used a PC based post-processor to visualize the results by injecting 5 particles every 0.08 second, so that a continuous particle stream was simulated. The particle diameter used in the calculation was 70 μm .

Case 1

Pulverized coal particles were down fired from a 0.39 meter diameter tube along with 15% of the combustion air. The secondary air which comprises the remainder of the total air entered through a 1.27 meter annulus. The vector plot of the mean gas velocity is shown in Figure 2a and the particle dispersion in Figure 2b. As expected, there was a large recirculation zone in the top part of the reactor. The positive radial velocity along with the turbulence caused a large scale particle dispersion in this case. Significant numbers of particles reached the refractory wall.

Case 2

This case is displayed as a comparison to Case 1. Two additional inlets, secondary II and tertiary, were added in order to shield the ceramic heat exchanger tubes from the coal and ash particles. The tertiary gas stream was pre-mixed CH_4 and air which entered through the outer annulus behind the heat exchanger tubes. To provide a buffer between the tubes and the flame, 2/3 of the secondary air was injected from secondary II and 1/3 of it entered from the secondary I. The secondary II inlet was approximately 0.25 meters in front of the heat exchanger tubes.

Figure 3a displays the gas flow pattern for this case and Figure 3b is the particle dispersion. The flow pattern obtained was considerably different from that obtained in Case 1 (Figure 2a). This is due to the added gas flux from the tertiary and the secondary II inlets. It demonstrates that firing schemes can effectively control the gas flow pattern. The particle dispersion near the wall region was much reduced in this case compared to Case 1. However, there were still a number of particles reaching the refractory wall at the bottom of the reactor.

Discussions

The three major mechanisms of particle transport in a gas flow are transport by the background mean gas flow, turbulence dispersion, and the initial particle spray angle. The spray angle can be controlled by using converging and diverging nozzles. In this work, we have demonstrated that the gas flow pattern is controllable by employing special firing schemes. For the current geometry, we can effectively use the buffer air to provide some protection of the heat exchange tubes from the corrosive and erosive coal particles.

For Case 2, turbulence dominates the particle dispersion. Particle dispersion is then controlled by the shape and the position of the zone with high turbulence intensity. In combustion, it is closely related to the shape and the size of the flame. With the current axial symmetry geometry, this zone seems not to be affected significantly by the air flow and firing schemes. However, with an appropriately tailored reactor geometry, the shape of the turbulence zone can be controlled and the particle dispersion can be redirected. This concept is shown in Figure 4 with a rectangular shaped reactor. When the cleaning air inlets are added, the flame shape will be affected so that less particle turbulence dispersion will be directed toward the heat exchange tubes. Selecting an appropriate shape for the coal conduit can help to achieve the flame shape control.

In two other cases(not shown here), the effect of swirl in the secondary inlet was investigated. Results showed that swirl must be avoided in the REACH reactor since the tangential motion created by the swirl causes large scale particle dispersion.

For the REACH reactor, attention must also be paid to the radiative heat exchange from the combustion flame to the heat exchange tubes and the convective heat transfer from the tube wall to the working fluid [6]. In parallel to CFD modeling of the particle turbulence dispersion in the REACH reactor, experimental investigation of both the radiation heat transfer and the aerodynamic cleaning effect was performed and results will be published elsewhere [6].

Acknowledgment

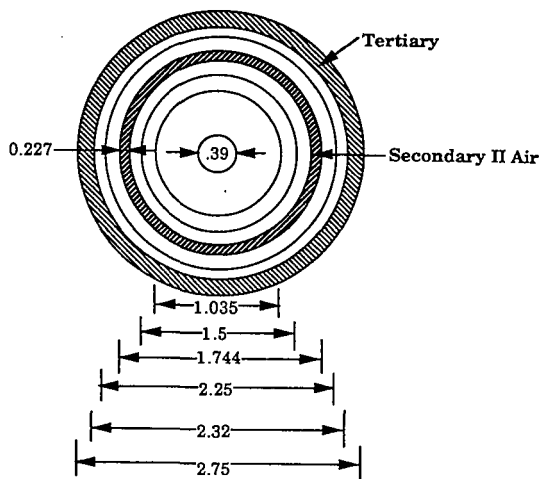
This work was supported by the Department of Energy, Pittsburgh Energy Technology Center through contract No. DE-AC22-92PC92196 managed by Clifford Smith and by the Department of Energy through contract No. DE-FG05-92ER81323. We acknowledge the assistance of Dr. B. Scott Brewster of Brigham Young University on the numerical modeling with PCGC-2, and the discussions with Dr. Steve J. Shamroth and Mr. Richard C. Buggeln of Scientific Research Associates, Inc.

References

1. Lockwood, F. C., Salooja, A. P., and Syed, S. A., "A Prediction Method for Coal-Fired Furnaces," *Combust. Flame*, **38**, 1 (1980).
2. Smith, P. J., Fletcher, T. J., and Smoot, L. D., "Model for Pulverized Coal-Fired Reactors," 18th Symp. (Int.) on Combustion, Combustion Int. Pittsburgh, 1185(1981).
3. Yuu, S., Yasukouchi, N., Hirose, Y., and Jotaki, T., "Particle Turbulence Diffusion in a Dust Laden Round Jet," *AIChE J.*, **24**, 509(1978).
4. Shuen, J.-S., Chen, L.-D., and Faeth, G. M., "Evaluation of a Stochastic Model of Particle Dispersion in a Turbulent Round Jet," *AIChE J.*, **29**, 167(1983).
5. Jang, D. S. and Acharya, S., "Calculation of Particle Dispersion Due to Turbulence in Elliptic Flows," *AIChE J.*, **34**, 514(1988).
6. Solomon, P. R., Serio, M. A., Cosgrove, J. E., Pines, D. S., Zhao, Y., Buggeln, R. C., and Shamroth, S. J., "A Coal Fired Heat Exchanger for An Externally Fired Gas Turbine," manuscript in preparation to J. Eng. Gas Turb. & Power, Trans. ASME, 1993.
7. *User's Manual, 93-PCGC-2: Pulverized Coal Gasification and Combustion Model (2-Dimensional) with a Generalized Coal Reactions Submodel (FG-DVC)*, Brigham Young University and Advanced Fuel Research Inc., 1993.
8. Sobczyk, K., *Stochastic Differential Equations*, Kluwer Academic Publishers, Boston, 1990.
9. Kloeden, P. E. and Platen, E., *Numerical Solution of Stochastic Differential Equations*, Springer-Verlag, New York, 1992.

Table 1. Flow conditions of Case 1 and 2.

		Flow Rates, Kg/s	
		Case 1	Case 2
Primary	Coal	0.50	0.50
	Air	0.88	0.88
Secondary I	Air	4.96	1.65
Secondary II	Air	-	3.31
Tertiary	CH ₄	-	0.067
	Air	-	1.34



Summary

Primary Air and Coal	= 0.39 m
Secondary I Air	= 1.035 m
Secondary II Air	= 1.744 m
Flame	= 1.5 m
U-Tubes	= 2.25 m
Reactor	= 2.75 m

Figure 1. REACH-exchange reactor, Top View.

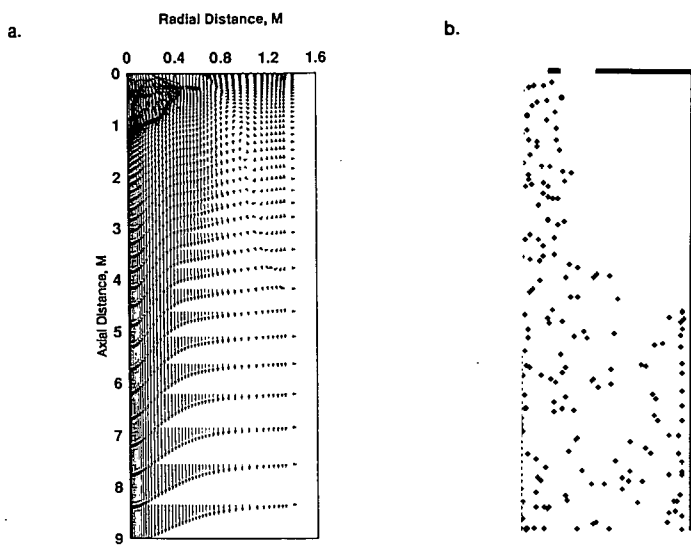


Figure 2. a. Velocity vector plot and b. particle dispersion of Case 1.

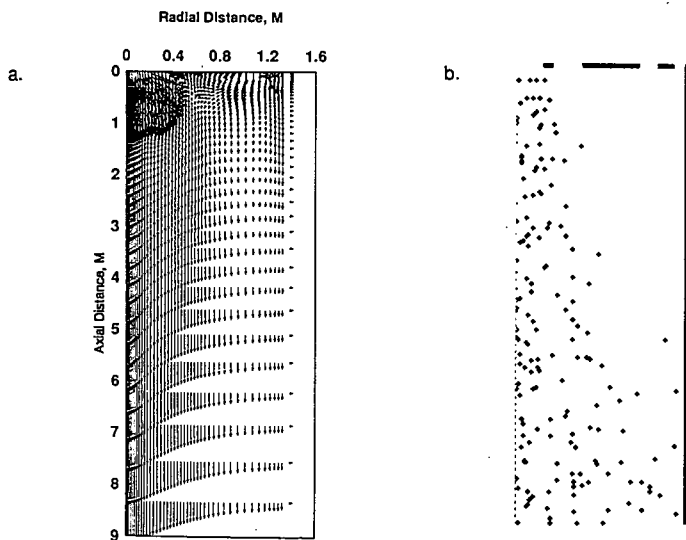


Figure 3. a. Velocity vector plot and b. particle dispersion of Case 2.

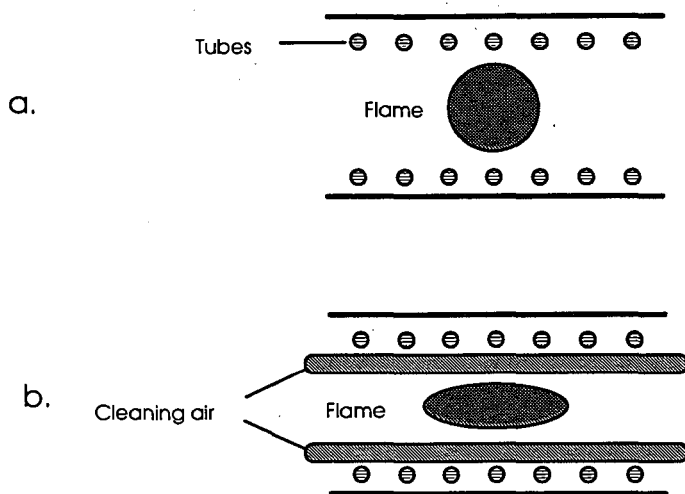


Figure 4. Top views of a rectangular REACH reactor, showing the effect of cleaning air on the shape of the flame. a. without the cleaning air and b. with the cleaning air.

The Modelling of the Particle/Turbulence Interaction for Oil and Coal-Fuelled Combustors

F.C. Lockwood, C. Papadopoulos and S.A.L. Perera

Department of Mechanical Engineering,
Imperial College of Science, Technology and Medicine,
London SW7 2AZ, United Kingdom.

Key words: Particle dispersion, correlation coefficient, evolving probability

INTRODUCTION

Most of the existing predictive codes rely on a stochastic treatment of the particle-turbulence interaction in which the trajectories of particles of finite number of representative sizes emerging from representative starting locations are computed. To obtain statistically reasonable results for position and velocity probability density functions (pdfs), more than 1000 particles from each size group and starting location must be tracked, thus they are not attractive in terms of computer economy.

The "Prediction of Evolving Probability (PEP)" model is a novel method developed by Lockwood and Papadopoulos⁵ to predict the evolution in time of the particles velocity pdf for two-phase flows. Given the gas conditions at the current particle position, the model predicts the particles velocity pdf for the chosen time step which gives the particle position.

In the present work PEP model is incorporated in the 2D-code FAFNIR in which the treatment of gas phase is based on the standard k-ε model. The calculation of the turbulent flow with the dispersed particulate phase is based on a statistically steady Eulerian framework for the motion of the carrier continuum phase and a Lagrangian simulation of the particulate phase.

Gas Flow Field

The gas flow is described by transport equations for mass, momentum and turbulence quantities which can be cast in the general form applicable to 2D, steady, non swirling, axisymmetric geometries:

$$\frac{\partial}{\partial x_i}(\rho U_i \phi) = -\frac{\partial}{\partial x_i}(\Gamma_{eff} \frac{\partial \phi}{\partial x_i}) + S_\phi + S_\phi^p \quad [1]$$

where U_i is the velocity component in direction x_i , the implied summation being restricted to the axial and radial components; ϕ represents any of the variables U, V, k, ϵ or h . The S_ϕ and Γ_{eff} are, respectively, the 'source' and the effective diffusion coefficients for the entity ϕ , while S_ϕ^p represents the particular source due to the presence of the particulate phase. The continuity equation is obtained by setting $\phi=1$ and $\Gamma_{eff}=1$.

The interaction with the dispersed particulate phase which is represented by S_ϕ^p is obtained using the 'Particle Source in Cell (PSIC)' method, Crowe et al¹, where the cells are the finite difference control volumes of the discretised flow domain for the gas phase calculation. These terms are calculated by the integration of all particle trajectories crossing a given control volume. The turbulence scales k and ϵ are obtained using the standard k-ε model equations and constants, Launder and Spalding⁴.

Particle Flow Field

The Lagrangian form of the governing equations for the particulate phase are analytically solved to predict the evolution in time of the particles velocity pdf. The instantaneous acceleration of a particle immersed in a gas at time t , in its non-linearised form, may be expressed as:

$$\frac{du_p(t)}{dt} = \frac{\rho_g A_p C_D}{2m_p} \text{SIGN}[u_g(t) - u_{pt}(t)]^2 + F_p \quad [2]$$

The particle drag coefficient, C_D , in general is a function of the Reynolds number based on gas-particle relative velocity. The following drag law has been employed for the present study.

$$C_D = \begin{cases} (1.0 + 0.15 \text{Re}_p^{0.687}) / (\text{Re}_p / 24) & \text{for } \text{Re}_p \leq 1000 \\ 0.44 & \text{for } \text{Re}_p > 1000 \end{cases}$$

SIGN signifies the sign of the relative velocity of the particle with respect to the gas. F_p is the sum of all forces acting on the particle excluding viscous force expressed by the first term on the right hand side. Only the viscous term is retained for the present formulation which neglect the following:

1. Inertial apparent force and Basset force.
2. Static pressure gradient force in the direction of motion.
3. Buoyancy effects.
4. Magnus effect as the particles are assumed to be non-rotating.

5. Particle-particle interaction.

With a closure assumption that the pdf of the gas velocities is Gaussian given that the pdf for the particle velocity is also Gaussian for the same spatial position and time, see Snyder and Lumley⁶, Wells and Stock⁹ and Tsuji and Morikawa⁷, the equation for the pdf of the ensemble particle velocity at time t , $P(v_p, t)$ is derived as, Lockwood and Papadopoulos⁵:

$$C[C_1 + C_2 v_p + C_3 v_p^2]P_{v_p} + P_t + C[C_2 + 2C_3 v_p]P = 0 \quad [3]$$

where

$$C = \frac{\rho_g A_p C_D \text{SIGN}}{2m_p},$$

$$C_1 = \sigma_g^2(1 - \rho_{gp}^2) + \left(\bar{u}_g - \frac{\rho_{gp}\sigma_g\bar{u}_p}{\sigma_p}\right)^2,$$

$$C_2 = 2\left(\bar{u}_g - \frac{\rho_{gp}\sigma_g\bar{u}_p}{\sigma_p}\right)\left(\frac{\rho_{gp}\sigma_g}{\sigma_p} - 1\right),$$

$$C_3 = \left(\frac{\rho_{gp}\sigma_g}{\sigma_p} - 1\right)^2.$$

P stands for the pdf $P(v_p, t)$ and the subscripts v_p and t denote the partial derivatives with respect to the subscripts. σ is the standard deviation of velocity fluctuations and subscripts g and p refers to gas and particulate phases respectively. v_p denotes the particle velocity in probabilistic space while u_g and u_p denote the mean values of velocity in real space. ρ_{gp} is the correlation coefficient for the gas-particle velocity fluctuations.

The solution of the equation [3] using method of characteristics is given by

$$P(v_p, t) = P_0 \left[\frac{q^{0.5}}{2C_3} \tan^{-1} \left(\frac{2C_3 v_p + C_2}{q^{0.5}} - \frac{C q^{0.5} t}{2} \right) \right] \frac{\left[\cos \left(\tan^{-1} \frac{2C_3 v_p + C_2}{q^{0.5}} \right) \right]}{\left[\cos \left(\tan^{-1} \frac{2C_3 v_p + C_2}{q^{0.5}} - \frac{C q^{0.5} t}{2} \right) \right]} \quad [4]$$

where $P_0(\dots)$ stands for the particle velocity pdf at time $t=0$.

Solution Procedure

Turbulent dispersion of the particles is simulated by sampling the gas phase properties at the current particle position at the beginning of each time step. The fluctuating component of the sampled gas velocity is assumed to be Gaussian with zero mean, for which the standard deviation is given by $\sigma_g = \sqrt{2k/3}$, Gosman and Ioannides², where k is the turbulent kinetic energy.

The fluctuating component of the particulate velocity is also treated in a similar manner where the mean particle velocity and its standard deviation are either known as initial conditions or taken from the previous iteration.

The velocity distributions for both the gas and particulate phases are generated analytically at the beginning of each time step with a range of 8σ , Papadopoulos⁸. The range of the most probable particle velocities is discretised into a number of regions of equal width, 20 in the present study, and a representative velocity is assigned to each division. At the end of the time step, values of the evolved representative velocities are sorted with the associated pdf values and these new values are used to calculate the moments of the new particle velocity distribution.

The overall solution procedure for the fluid flow and the particle phase is as follows:

1. A converged solution of the of the gas flow field is calculated without the source terms of the dispersed phase.
2. Representative parcels of particles starting from a finite number of starting locations are traced through the flow field to obtain the mean trajectories and source terms.
3. The flow field is recalculated by considering the source terms of the dispersed phase, where appropriate considering the underrelaxation factors.
4. Repetition of steps 2 and 3 until convergence is reached.

Results and Discussion

Particle motion in a laminar flow is a special case where the gas-particle velocity correlation coefficient and the root mean square(rms) value of the velocity fluctuations are zero, thus giving a simplified solution of the equation [4].

Figure 1 presents the development of the particle velocity in a uniform laminar flow field of mean velocity 10.0m/s. Initial mean particle velocity and its rms value are assumed to be 9.0m/s and

0.5m/s respectively. The rms value of the initial Gaussian distribution of particle velocity diminishes with time to approach a delta function at longer times centred as expected on the mean gas velocity.

Figure 2 shows the turbulent response of three particle size groups 15 μ m, 40 μ m and 100 μ m respectively. The special analytical solution of the equation [4] is used for the case of $\rho_{gp}=1.0$. A free turbulent jet of mean exit velocity 10.0m/s and rms value 0.4m/s is used. Initial mean particle axial velocity and its rms value are assumed to be 9.0m/s and 0.5m/s respectively for all three size groups. It is evident from the figures, that smallest size group tend to follow the mean gas motion whereas the high inertia of the 100 μ m particles shows a slower response.

On the basis of the evidence presented above and the other supporting evidence by Lockwood and Papadopoulos⁵, the PEP model may be applied to a real physical flow field for which experimental data exist.

Detailed measurements of particle dispersion in a round free jet constitutes a reliable reference for validation of a particle dispersion model because gas velocity profiles and turbulent properties can be simulated accurately with the standard k- ϵ model. Hardalupas et al⁹ provides useful measurements for the gas and particulate phases in a round free jet. In the present study, velocity predictions using the PEP model are compared with the experimental measurements, taken using a phased-LDA, for a round, unconfined two-phase jet flow reported by Hardalupas et al⁹.

A downward directed jet, exhausting into ambient air environment is used. The flow develops in a 15mm diameter precision bore stainless steel tube for 50mm before exhausting into ambient air.

Due to symmetry, only a half of the flow field is considered. A computational area of 0.5m in radius and 3m in length [Figure 3] with a non-uniform grid of 37*51 is used to simulate the flow field. Outside the injection pipe, the entrainment air flow is initialised to a low velocity, sufficient to prevent recirculation within the flow field.

According to the measurements, the initial velocity of the particles is set to 90% of the mean jet gas exit velocity of 13.1m/s. Particles of 40 μ m diameter and 2420kg/m³ density are released from 10 radial positions at the exit of the injection pipe. The jet exit Reynolds number is 13000 with a mass loading of 13%.

Figure 4 shows the centreline variation of the mean axial velocity and its rms value for the particulate phase. Figure 5 presents the radial profiles of the mean particle axial velocity at three axial stations. Predictions using the PEP model with gas-particle velocity correlation coefficient values of 0.1, 0.5 and 1.0 are tested. A gas-particle velocity correlation coefficient of 1.0 gives better overall predictions although the dispersion effect is underpredicted. Considering the results at the first axial station ($x/d=10$), it is evident that a low correlation coefficient value near the jet exit region gives a much better response to turbulence.

Figure 6 presents a comparison between the performance of the PEP model with that of a stochastic model similar to one used by Gosman and Ioannides². With stochastic model 25 stochastic trials are performed for each particle group. It is clear that the radial profiles of mean axial velocity and its rms value are better predicted by the PEP model with a correlation coefficient of 1.0, although the dispersion is underpredicted. Under prediction of the dispersion can be directly attributed to the use of a constant correlation coefficient value for the whole flow domain at the present state. Analytical determination of the gas-particle correlation coefficient at each sampling location may lead to much superior predictions, but this matter is beyond the scope of the present paper.

A test simulation has been performed imposing an arbitrary linear variation on the value of the correlation coefficient. It is set to 0.2 at the jet exit and increased linearly with axial position to 1.0 at $x/d=25$ and then allowed to remain constant. As expected, the dispersion effect is clearly improved [Figure 7].

CONCLUSIONS

The effective coding of the PEP model is successfully completed. Predictions of the PEP model are superior to those of the stochastic model and result in a considerable reduction in computational time. Reproducibility of the results is an added advantage of the present formulation over the conventional stochastic simulations with random number generation. Given the possibility of analytical determination of the gas-particle velocity correlation coefficient still better predictions will be achievable with the present formulation.

References

1. Crowe, C.T., Sharma, M.P., and Stock, D.E., "The Particle-Source-in Cell (PSI-Cell) Model for Gas Droplet Flows", *Journal of Fluid Engineering*, (1977), pp. 275-332.
2. Gosman, A.D. and Ioannides, E. (1983). "Aspects of computer simulation of liquid fuelled combustors", *Journal of Energy*, Vol. 7, No. 6, p. 482.

3. Hardalupas, Y., Taylor, A.M.K.P., and Whitelaw, J.H. (1988), "Velocity and particle flux characteristics of turbulent particle laden jets", Imperial College, Mechanical Engineering Department, Fluids Section, Report FS/87/14.
4. Launder, B.E. and Spalding, D.B., The numerical computation of turbulent flows., Comp. Meth. Appl. Mech. and Eng., 3(1974), pp.269-289.
5. Lockwood, F.C. and Papadopoulos, C. (1989). "A new method for the computation of particulate dispersion in turbulent two-phase flows", Combustion and Flame, Vol 76, pp. 403-413.
6. Lumley, J.L. and Snyder, W.H. (1971), "Some measurements of particle velocity autocorrelation functions in a turbulent flow", Journal of Fluid Mechanics, Vol.48, p.41.
7. Morikawa, Y. and Tsuji, Y. (1982), "LDV measurements of an air-solid two-phase flow in a horizontal pipe", Journal of Fluid Mechanics, Vol.120, p. 385.
8. Papadopoulos, C. (1989), PhD Thesis, University of London.
9. Stock, D.E. and Wells, M.R. (1983), "The effects of crossing trajectories on the dispersion of particles in a turbulent flow", Journal of Fluid Mechanics, Vol.136, p. 31.

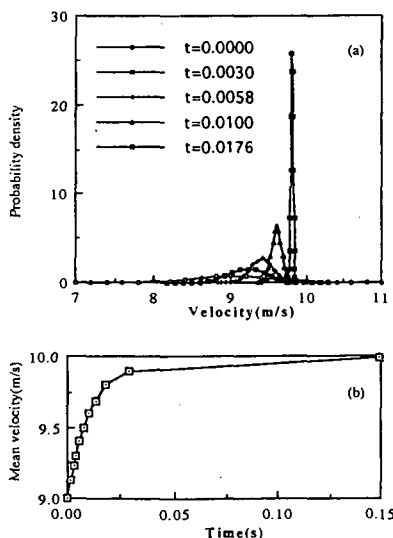


Figure 1: Particles of 40µm diameter in a uniform laminar flow, Gaussian velocity distribution at injection. (a) Evolution of velocity pdf in time, (b) mean velocity.

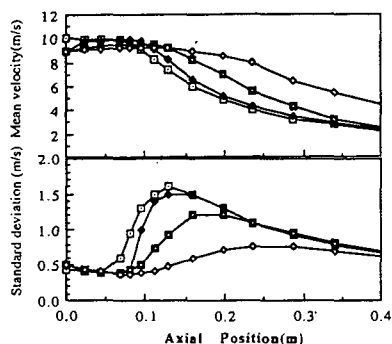


Figure 2: Response of particle phase to fully turbulent flow. Predictions using PEP model for particle diameters; \circ 15µm, \blacksquare 40µm and \triangle 100µm, \bullet local gas velocity.

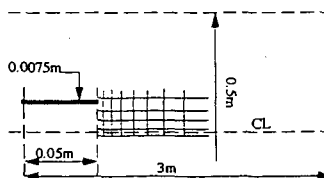


Figure 3: Computational domain. Nonuniform grid of 51*37

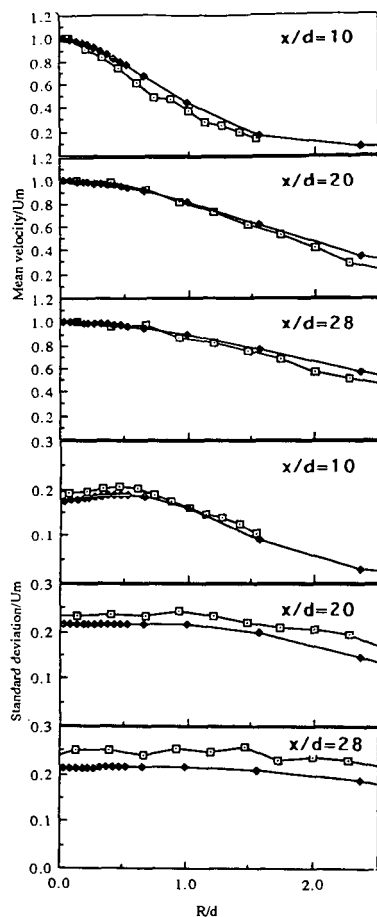


Figure 4: Predicted and measured radial profiles of mean axial velocity and standard deviation for single phase jet. \square measurements, \blacklozenge predictions. Results normalised by centreline axial velocity, U_m .

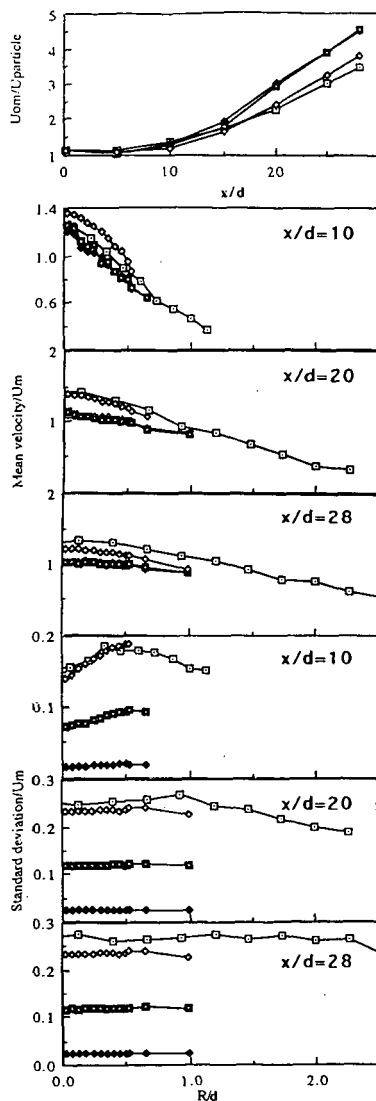


Figure 5: Predicted and measured mean axial velocity and standard deviation. (a) centreline profile, (b) radial profile [at three axial stations] for particle phase. \square measurement. Predictions with velocity correlation coefficient \blacklozenge 1.0, \blacklozenge 0.5 and \blacklozenge 0.1. Results normalised by centreline mean axial velocity, U_m , and jet exit velocity, $U_{m,0}$, for clean jet.

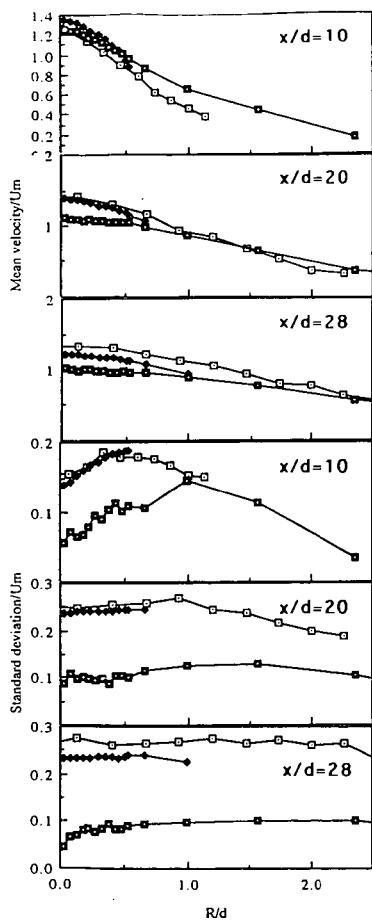


Figure 6: Predicted and measured radial profiles of mean axial velocity and standard deviation [at three axial stations] for particle phase. \square measurement. Predictions: \blacklozenge PEP model with $pgp=1.0$, \blacksquare stochastic model. Results normalised by clean jet centre-line axial velocity, U_m .

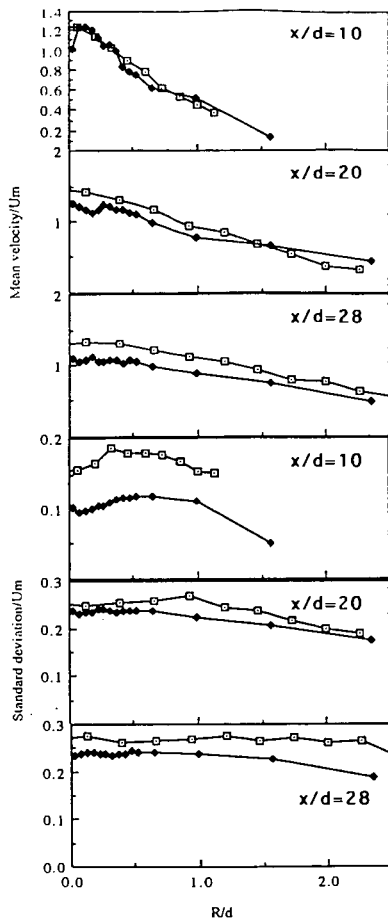


Figure 7: Predicted and measured radial profiles of mean axial velocity and standard deviation [at three axial stations] for particle phase. \square measurement \blacklozenge PEP model with a linearly varying velocity correlation coefficient. Results normalised by clean jet centreline axial velocity, U_m .

Droplet Motion under the Influence of Flow Nonuniformity and Relative Acceleration

F. PENG AND S. K. AGGARWAL

Department of Mechanical Engineering, University of Illinois at Chicago
Chicago, Illinois 60680

Abstract

A computational study on the dynamics of single droplets is performed in two gas flows at moderately higher Reynolds numbers, one is Poiseuille flow in which gas is either nitrogen or helium and the other one is counterflow formed by two opposed streams of nitrogen. The focus of the study is to review the methodologies used for representing the effects of flow nonuniformity and relative acceleration on droplet motion in moderately high Reynolds numbers. The motion of the droplets is observed to be affected by the flow nonuniformity and unsteadiness, characterized respectively by dimensionless parameters κ and A_c , and the effects due to nonuniformity and rate of change of relative velocity are separable. It is determined that acceleration and deceleration affect the drag and lift on droplets in dissimilar ways. The lift force caused by flow nonuniformity is in the same direction of κ in Poiseuille flow, whereas it is in the opposite direction of κ in counterflow. It is noted that the radius of curvature of droplet trajectory affects lift force more strongly than drag force. Modified correlations for the drag and lift coefficients as function of the Reynolds number and dimensionless parameters characterizing the flow nonuniformity and unsteadiness are proposed.

Keywords: drag, lift, unsteady, nonuniformity

NOMENCLATURE

A_c	Acceleration factor	m	Mass
C_A	Added-mass drag coefficient	Re	Droplet Reynolds number, $Re = D_d V_r / \nu_g$
C_D	Drag coefficient	u_i	Velocity component in i-direction
C_{Ds}	Steady-state drag coefficient	V_r	Magnitude of relative velocity
C_H	Basset history drag coefficient	x_i	Displacement in i-direction
C_L	Lift coefficient	ρ	Density
D_d	Droplet diameter	μ	Viscosity
d_{ij}	The deformation rate tensor	ν	Kinematic viscosity
g	Gravity	κ	Nonuniformity factor
K	The coefficient of Saffman's lift force		

Subscripts

g	Gas	i=1	Radial direction
d	Droplet	i=2	Axial direction

1. Introduction

One aspect of spray computation research which remains mostly unexplored is the accurate representation of the drag and lift forces operative on droplets as they undergo a highly complex, curvilinear, unsteady motion on a turbulent flow field. The droplet dynamics models being used currently in spray computations consider the standard drag force only; the effects of flow nonuniformity and droplet relative acceleration on the droplet drag and lift forces are not considered. In addition, the effect of unsteadiness on the motion of a droplet traveling in a curvilinear trajectory is not considered. A number of studies (Clift et al., 1978, Leal, 1980, and Puri and Libby, 1989, 1990) have found that these effects can significantly alter the droplet motion by changing the net drag force and introducing a significant lift force. Clearly, the trajectories obtained without consideration of these forces can be a significant source of error in a comprehensive spray computation.

In the analysis of multiphase flows, the particle shape is often assumed to be spherical for simplicity and the drag on a sphere is thought to have been well-understood at low Reynolds numbers. Many researchers have sought a general equation of motion to determine the trajectory of droplets in an unsteady, nonuniform flow. Originally Basset (1888), Boussinesq (1885), and Oseen (1927) developed a force expression, known as BBO equation, for a slowly moving, accelerating, rigid sphere in a still fluid. Later, Tchen (1947) extended the BBO equation to incorporate the effects of a temporally varying flow field on particle transport. Corrsin and Lumley (1956) modified Tchen's equation to account for spatial nonuniformity of the flow field. Riley (1971) revised Corrsin and Lumley's equation to properly account for the effect of the undisturbed flow on a particle's motion. Maxey and Riley (1983) modified the equation of Tchen (1947), and they suggested the following equation for a small rigid sphere in a nonuniform flow:

$$\begin{aligned} \frac{du_{di}}{dt} = & \frac{3}{4} \frac{\rho_g}{\rho_d} \frac{C_{Dg}}{D_d} V_r \cdot (u_{gi} - u_{di} + \frac{1}{24} D_d^2 \nabla^2 u_{gi}) + \frac{\rho_g}{\rho_d} \frac{Du_{gi}}{Dt} + \frac{1}{2} \frac{\rho_g}{\rho_d} \frac{d}{dt} (u_{gi} - u_{di} + \frac{1}{40} D_d^2 \nabla^2 u_{gi}) \\ & + \frac{\rho_g}{\rho_d} \sqrt{\frac{81\nu_g}{\pi D_d^2}} \int_0^t \frac{1}{\sqrt{t-t'}} \frac{d}{dt} (u_{gi} - u_{di} + \frac{D_d^2}{24} \nabla^2 u_{gi}) dt' + (1 - \frac{\rho_g}{\rho_d}) g_i \end{aligned} \quad (1)$$

The derivative d/dt denotes a time derivative following the moving sphere, and the derivative D/Dt the time derivative following a fluid element. The terms on the right hand side correspond in turn to the effects of viscous Stokes drag, pressure gradient of the undisturbed flow, added mass, Basset history term, and buoyancy.

The modified BBO equation and the above equation have been widely used for the study of the motion of small droplets in a fluid (Lázaro and Lasheras, 1989, and Liang and Michaelides, 1992). It should be noted, however, that both the equations are restricted to the Stokesian flow or "creeping flow", since the convective terms are omitted in their derivation. Unfortunately, no theoretical expression is available for the force on droplet at higher Reynolds number, if the effects like rotation, flow nonuniformity, and unsteadiness are added to the problem. Thus, some experimental work has been done to study the effects of flow nonuniformity and droplet acceleration at higher Reynolds number separately.

Odar and Hamilton (1964) used an experimental study and obtained correlations for the effects of added mass term and Basset history term at Reynolds number values up to 62. They expressed the total drag force by the use of the empirical coefficients C_{Ds} , C_A and C_H :

$$m_d \frac{du_d}{dt} = C_{Ds} \cdot \frac{\pi}{4} D_d^2 \cdot \frac{1}{2} \cdot \rho_s V_r (u_{gr} - u_d) + C_A \cdot \frac{\pi}{6} D_d^3 \rho_s \frac{d}{dt} (u_{gr} - u_d) + C_H \cdot \frac{D_d^2}{4} \cdot \sqrt{\pi \rho_s \mu_s} \cdot \int_0^t \frac{d}{dt} (u_{gr} - u_d) \cdot \frac{dt}{\sqrt{t-t'}} \quad (2)$$

where C_{Ds} , C_A and C_H are, respectively, the steady-state, added-mass and history drag coefficients. C_{Ds} is defined later in Eq. (14). Based on their measurements, Odar (1966) suggested the empirical formulas for C_A and C_H by introducing a nondimensional acceleration parameter A_c .

Odar (1966) confirmed that the empirical formulas for C_A and C_H , derived for a simple harmonic motion, are valid for the free fall of a sphere in a viscous fluid. Hughes and Gililand (1952) and Hjelmfelt and Mockros (1967) also predicted that a sphere which falls freely experiences drag higher than that given by the Stokes coefficient as it accelerates to its terminal velocity for higher Reynolds number. Tsuji and Tanaka (1990) investigated the drag on a sphere in a periodically pulsating flow experimentally for Reynolds number in the range $8000 < Re < 16,000$. Their results show that the drag increases in the accelerating flow and decreases in the decelerating flow. Odar (1968) provided data on the drag of a sphere along a circular path in the Reynolds number range from 6 to 185, which shows that the effects of the added mass and the history of the motion increase for this case whereas the contribution from the steady-state drag remains the same as that in a rectilinear motion. Contrary to the above, there is another group of works showing the opposite results. For instance, Temkin and Kim (1980) and Temkin and Melta (1982) obtained the drag by observing the motion of sphere in a shock tube and modified the drag coefficient C_D including the effects of unsteadiness. Their results show that acceleration decreases and deceleration increases droplet drag. Besides Temkin and Kim (1980) and Temkin and Mehta (1982), Ingebo (1956) reported results showing the same trend.

A thorough review of the effects of flow nonuniformity on particle motion is given by Clift (1978) and Isele (1980). The additional force caused by flow nonuniformity may be decomposed into a drag force in the direction of relative velocity and a lift force normal to the drag. In order to develop useful correlations, the effect of flow nonuniformity is usefully represented in terms of a nondimensional parameter κ and the droplet Reynolds number (Puri and Libby, 1990). Eichhorn and Small (1964) suspend large spheres in a Poiseuille flow at several inclinations of the tube and obtain lift and drag data in the Reynolds number range of 80 to 250. Saffman (1965) studies theoretically the lift on a small sphere in a slow shear flow. Dandy and Dwyer (1988) present numerical simulation for a neutrally buoyant spherical particle in a steady, linear shear flow over a Reynolds number range of ten to one hundred. Their results indicate that for a given rate of shear, the lift coefficient is inversely proportional to the square root of the Reynolds number for lower Reynolds number (less than ten) and constant at higher Reynolds number. Puri and Libby (1990) conduct experiments on droplets moving in a Poiseuille flow in the Reynolds number range of 0.7 to 27 and κ in the range of 10^{-3} to 6×10^{-2} and determined that the droplets experience drag larger than that indicated by the standard drag. Following the reasoning of Drew (1978) they attribute this increase in the drag to the effects of flow nonuniformity and empirically correlate the increase in drag and lift coefficients.

In spite of the abundance of literature on the effects of flow unsteadiness and nonuniformity, there are no previous correlation to calculate the drag and lift forces affected simultaneously by both flow nonuniformity and relative acceleration at higher Reynolds number. In the present paper, a computational study of motion of droplets in Poiseuille flow and counterflow is reported. The major focus of the study is to present a detailed comparison of the droplet trajectories predicted by five different approaches with the experimental data of Puri and Libby (1990, 1989) and to propose modified correlations for the effects of flow nonuniformity and relative acceleration at moderately high Reynolds number.

2. The Physical Situation

The droplet motions in Poiseuille flow and counterflow are studied. The flowfields are identical to those of Puri and Libby (1990) and Puri and Libby (1989), and the reader is referred to their study for a detailed description. A Poiseuille flow is established in either nitrogen or helium at room temperature in a vertically mounted quartz tube of length 1.83 m and inner diameter of $2R=2.14$ cm. Liquid droplets in an upward flowing Poiseuille flow of gases experience a downward velocity relative to the flow. A counterflowing flowfield is established by flowing gaseous nitrogen from two opposed ducts. The ducts have a radius of 2.3 cm and are placed 1.5 cm apart. The flow exits each duct with a discharge velocity of 31.7 cm/s. A droplet generator, the nozzle of which is placed in the bottom duct, introduces n-heptane droplets of 100 and 130 μm diameter into the gas stream just before it enters the counterflow. The flowfield is described by Libby et.al. (1989). The accuracy of the gas velocity components is confirmed by comparison with the experimental results of Chen et al. (1987) and the LDV measurements of Puri and Libby (1989).

3. The Equation of Motion

As reviewed above, several different approaches have been used in the past to represent the effects of acceleration and flow nonuniformity on droplet motion. The following approaches are employed in this paper.

Approach (1): The equation of motion, based on Eq.(1), in which the unsteady effect is introduced by using the empirical coefficients, C_A and C_H , and the lift force is included, is given as

$$\begin{aligned} \frac{du_{di}}{dt} = & \frac{3}{4} \cdot \frac{\rho_g}{\rho_d} \cdot \frac{C_{Dz}}{D_d} V_r \cdot (u_{gi} - u_{di}) + \frac{\rho_g}{\rho_d} \frac{Du_{gi}}{Dt} + C_A \frac{1}{2} \frac{\rho_g}{\rho_d} \frac{d}{dt} (u_{gi} - u_{di}) \\ & + C_H \frac{\rho_g}{\rho_d} \sqrt{\frac{81V_g}{\pi D_d^2}} \int_{t_0}^t \frac{1}{\sqrt{t-t'}} \frac{d}{dt'} (u_{gi} - u_{di}) dt' + \frac{\rho_g}{\rho_d} \cdot \frac{2K\nu^{1/2} d_{ij}}{D_d (d_{ik} d_{il})^{1/4}} (u_{gi} - u_{di}) + \left(1 - \frac{\rho_g}{\rho_d}\right) g \end{aligned} \quad (3)$$

$$\frac{dx_i}{dt} = u_{di} \quad (4)$$

$K=2.594$ is the coefficient of Saffman's lift force, and the deformation rate tensor d_{ij} is defined as

$$d_{ij} = \frac{1}{2} (u_{gij} + u_{gji}) \quad (5)$$

where

$$u_{sji} = \frac{\partial u_{si}}{\partial x_j} \quad (6)$$

The expression of lift force used in Eq.(3) is a generalization of the expression provided by Saffman (1965) for three-dimensional shear fields, which is restricted to small droplet Reynolds number. In addition, the droplet Reynolds number based on the relative droplet velocity must also be smaller than the square root of the droplet Reynolds number based on the shear field. The formulas suggested by Odar (1966) are used to calculate C_A and C_H .

Approach (2): Following the equations suggested by Temkin and Mehta (1982) and others, the effect of unsteadiness is considered by modifying the drag coefficient C_D . The effect of flow nonuniformity on drag and lift is, however, represented in a manner similar to approach (1).

$$\frac{du_{di}}{dt} = \frac{3}{4} \cdot \frac{\rho_g}{\rho_d} \cdot \frac{C_D}{D_d} V_r \cdot (u_{si} - u_{di}) + \frac{\rho_g}{\rho_d} \frac{Du_{si}}{Dt} + \frac{\rho_g}{\rho_d} \cdot \frac{2Kv_s^{1/2} d_{ij}}{D_d (d_{ik} d_{il})^{1/4}} (u_{sj} - u_{dj}) + (1 - \frac{\rho_g}{\rho_d})g \quad (7)$$

d_{ij} and u_{sji} are the same as defined above.

Approach (3): The effects of flow nonuniformity and unsteadiness are represented in terms of additional lift and drag coefficients. If we assume that both lift and drag forces influence the droplet, then the force on the droplets acceleration components in the radial and axial directions are:

$$\frac{du_{d1}}{dt} = \frac{3}{4} \cdot \frac{\rho_g}{\rho_d} \cdot \frac{V_r}{D_d} [-C_L(u_{s2} - u_{d2}) + C_D(u_{s1} - u_{d1})] \quad (8)$$

$$\frac{du_{d2}}{dt} = \frac{3}{4} \cdot \frac{\rho_g}{\rho_d} \cdot \frac{V_r}{D_d} [C_L(u_{s1} - u_{d1}) + C_D(u_{s2} - u_{d2})] \quad (9)$$

where C_L and C_D are the coefficients of lift and drag respectively.

Puri and Libby (1990) suggest the following correlation for drag and lift coefficients:

$$C_D = C_{Dv} (1 + 575 (\frac{\kappa^2}{Re})^{3/4}) \quad (10)$$

$$C_L = 20 C_{Dv} (\frac{\kappa^2}{Re})^{3/4} \quad (11)$$

Approach (4): The modified correlations proposed in the present study are:

$$C_D = C_{Dv} (1 + C_{KD} (\frac{\kappa^2}{Re})^{3/4}) - C_{AD} \cdot A_C \quad (12)$$

$$C_L = C_{KL} \cdot C_{Ds} \left(\frac{K^2}{Re} \right)^{3/4} - C_{AL} \cdot A_c \quad (13)$$

where C_{KD} , C_{AD} , C_{KL} and C_{AL} are constant.

In Poiseuille flow: $C_{AD} = 0.42$, $C_{AL} = 5 \times 10^{-3}$, when $A_c < 0.0$

$$C_{KD} = 575.0, C_{KL} = 50.0$$

In counterflow: $C_{AD} = 0.52$, $C_{AL} = 0.15$, when $A_c < 0.0$

$$C_{AD} = 0.2, C_{AL} = 0.15, \text{ when } A_c > 0.0$$

$$C_{KD} = 725.0, C_{KL} = 400.0$$

A_c is defined by Temkin and Kim (1980).

Approach (5): The fifth approach considers only the viscous and pressure drag represented by C_{Ds} . For low Reynolds number, C_{Ds} is given by the Stokes drag, whereas for high Reynolds number, it involves Stokes drag and a correction such as proposed by Putnam (1961), i.e.,

$$C_{Ds} = \frac{24}{Re} \cdot \left(1 + \frac{Re^{2/3}}{6} \right) \quad (14)$$

4. Results and Discussion

The fourth order Runge-Kutta method has been used to calculate the droplet velocity and displacement. The effects of flow nonuniformity and relative acceleration are investigated by studying the droplet trajectories and displacement histories in both radial and axial direction predicted by the five approaches and experimental data.

Figures 1 shows the droplet trajectories and displacement histories in both radial and axial directions predicted by above five approaches, and obtained experimentally in Poiseuille flow. Three cases have been considered and each case has different initial conditions, and also different droplet size or different fluid. In this paper only one case is shown. As seen in Fig. 1, the droplets introduced off the axis migrate toward the axis. Comparing the displacement histories in radial direction, it is noted that the values predicted by approach (5) are greater than those determined experimentally. In addition, the existence of a lift force which moves the droplet towards the axis is indicated. The sign of the lift force is the same as that given by Saffman (1965). Compared with experimental data, the approach (3) underpredicts the lift force whereas approach (1) and (2) overpredict the lift force. Note that the error in the trajectory prediction is mainly due to the inaccurate representation of the lift force. In approach (1) and (2), the lift force is evaluated by using the Saffman lift force expression, which is restricted to low Reynolds number situations. Approach (3), based on the correlation of Puri and Libby (1990), considers the flow nonuniformity effect, but may be improved further by including the acceleration effect. The modified equation (13) used in approach (4) includes the latter effect, and provides a better representation for the lift coefficient.

The droplet displacement in axial direction is influenced mostly by drag force. The larger the drag force, the shorter the distance traveled by the droplet in the axial direction, when droplets move in the

opposite direction of gas flow. As demonstrated in Fig.1, approach (1) and (2) underpredict the drag force. A plausible explanation for the underprediction of the drag force by approach (1) is that it employs correlations of Odar and Hamilton (1964), which are based on an experimental study of droplets in harmonic motion. If the droplet moves along a curved path, the unsteady effect will increase. As the result of curvilinear trajectory of droplets and inaccurate consideration of nonuniformity, the approach (1) underpredict the drag force. Similarly the error in using approach (2) is caused by an inappropriate application of the formula proposed by Temkin and Melta (1982) and Saffman (1965) lift force expression. In order to modify approach (3) which underpredicts the drag force, we include the unsteady effect. Consequently, the droplet trajectories as well as displacement histories in both radial and axial directions predicted by the modified correlation are in better agreement with those determined experimentally.

The droplets in counterflow experience a much more complex, curvilinear, and unsteady (including both acceleration and deceleration) motion. Two cases have been studied with different droplet size and initial condition. In case 1, droplet diameter is $100\text{ }\mu\text{m}$. In case 2, droplet size is $130\text{ }\mu\text{m}$, and the droplet initial velocity in axial direction is much higher than that in radial direction.

As noted from Figs.2 and 3, the trajectories predicted by approach (5) are much different from the experimental data, especially in radial direction, indicating lift force must be important in these cases. The presence of lift in a curvilinear trajectory is not surprising. In experiments on the motion of a sphere along a curvilinear path in the Reynolds number range of 30 to 80, Odar (1968) finds that the lift is as high as ten percent of drag. In their study on droplets in a counterflow, Puri and Libby (1989) contend that the droplets are influenced by the skewness of the acceleration vector from the relative velocity vector. As a result, the net force due to acceleration is not collinear with the relative velocity. Consequently, the consideration of acceleration effects in a curved trajectory requires that both the drag and lift due to acceleration must be calculated. The unsteady effect on drag and lift is given in Eq.(12) and Eq.(13). From these relations it is seen that the deceleration will increase drag force, and acceleration will decrease drag force. This is consistent with the results of Temkin and Mehta (1982).

It is known that the flow nonuniformity affects both drag and lift force. It is not clear, however, as to how the direction of lift force changes with the sign of κ . In Poiseuille flow, κ is always positive. According to Saffman, if the particle lags behind the fluid, a radially inward lift force exists causing their migration toward the tube axis. If, on the other hand, the particle travels faster than the fluid, the effect will move the particle away from the axis, i.e., the lift force coefficient follows the sign of κ . In counterflow, the plots of C_L and κ indicate that the direction of C_L is opposite to that of κ . In the present study, this observation is used to determine the sign of C_L in Eqs. (12) and (13).

For approach (4), comparing the constants C_{AD} , C_{AL} , C_{KD} , and C_{KL} in Poiseuille flow with those in counterflow, it is noted that the constants C_{AD} and C_{KD} used in calculating drag coefficient are not much different in the two flows. However, the constants C_{AL} and C_{KL} used in calculating lift coefficient are much larger in counterflow than those in Poiseuille flow. It indicates that the radius of curvature of droplet trajectory, which is much larger in Poiseuille flow than in counterflow, but change continuously along the droplet trajectory in the counterflow, may affect the lift force, and the larger the radius of the curvature of droplet trajectory, the less effect on the lift force. Finally, a plausible explanation for the departure of displacement histories in radial direction predicted by approach (4) and experimental data (Figs. 2(b) and 3(b)) is attributed to the fact that the correlations used in approach (4) do not consider the effect of changing curvature and skewness of acceleration vector along the droplet trajectory.

5. Conclusions

The droplet motion under the influence of flow nonuniformity and relative acceleration has been investigated in Poiseuille flow and counterflow. Several approaches that are currently in use for representing these effects have been evaluated. It is found that the application of Odar's formula, Temkin's formula and Puri and Libby's correlation is not accurate enough to predict the trajectories obtained from previous experimental studies. It is indicated that calculations of κ and A_c can be performed for both Poiseuille flow and counterflow, so that the effects due to nonuniformity and rate of change of relative velocity are separable. It is determined that acceleration and deceleration affect the drag on droplets in dissimilar ways, which is consistent with the results of Temkin and Mehta (1982). The lift force caused by flow nonuniformity is in the same direction of κ in Poiseuille flow, and in the opposite direction of κ in counterflow. It is seen that the radius of curvature of droplet trajectory affects lift force more strongly than drag force, and the larger the radius of the curvature of droplet trajectory, the less effect on the lift force. Modified correlations for the drag and lift coefficients as function of the Reynolds number and dimensionless parameters characterizing the flow nonuniformity and unsteadiness are proposed.

Since the correlations proposed in the present work is based on the analyses of the experimental data of Puri and Libby (1990, 1989), they may not be applicable to other situations that are significantly different from these experiments. The effects of the radius of curvature of droplet trajectory and the skewness of the acceleration vector from the velocity vector on the drag and lift force have not been studied in detail in the present work. Clearly, more experimental and theoretical studies are needed to analyze these effects on the drag and lift force.

Acknowledgments

This work has been supported by a grant from the NASA Lewis Research Center under the technical direction of D. Bulzan, Institute of Computational Mechanics in Propulsion (ICOMP). We thank Dr. I. S. Puri for helpful discussions.

References

- Basset, A. B., 1888, *A Treatise on Hydrodynamics*, Cambridge: Deighton, Bell and Co., Vol. 2, Ch. 21.
- Boussinesq, J. V., 1885, *Sur La Resistance . . . d'une Sphere Solide*, C. R. *des Seances de l'Academie*, Vol. 100, pp. 935.
- Chen, Z. H., Liu, G. E., and Sohrab, S. H., 1987, "Premixed Flames in Counterflow Jets under Rigid Body Rotation," *Combust. Sci. Tech.*, Vol. 51, pp. 39-50.
- Dandy, D. A and Dwyer, H. A., 1988, "Influence of Fuel Stream Vorticity on Particle Lift, Drag and Heat Transfer," Paper #WCS/CI 88, 1988 Fall Meeting of the Western States Section/ The Combustion Institute, Dana Point, California
- Drew, D. A., 1978, "The Force on a Small Sphere in Slow Viscous Flow," *J. Fluid Mech.*, Vol. 88, pp. 393-400.
- Eichhorn, R., and Small, S., 1964, "Experiments on the Lift and Drag of Spheres Suspended in a Poiseuille Flow," *J. Fluid Mech.*, Vol. 20, pp. 513-527.
- Hjelmfelt, A. T., Jr. and Mockros, L. F., 1967, "Stokes Flow Behavior of an Accelerating Sphere," *J. Engng. Mech. Div. (proc. ASCE)*, Vol. 93, No. EM687
- Ho, B. P., and Leal, L. G., 1974, "Inertial Migration of Rigid Spheres in Two-Dimensional Unidirectional Flows," *J. Fluid Mech.*, Vol. 65, pp. 365-400.
- Hughes, R. R., and Gilliland, E. R., 1952, "The Mechanics of Drops," *Chem. Engng. Prog.*, Vol. 48, pp. 497
- Ingebo, R. D., 1956, "Drag Coefficients for Droplets and Solid Spheres in Clouds Accelerating in Air Streams," NACA Technical Note, TN 3762
- Lázaro, B. J., and Lasheras, J. C., Jun. 1989, "Particle Dispersion in a Turbulent, Plane, Free Shear Layer," *Phys. Fluid A*, vol. 1, No. 6, pp. 1035-1044.

- Liang, L., and Michaelides, E. E., 1992, "The Magnitude of Basset Forces in Unsteady Multiphase Flow Computations," *J. of Fluids Engng.*, Vol. 114, pp. 417-419.
- Libby, P. A., Sivashinsky, G. I., and Williams, F. A., 1990, "Influences of Swirl on the Structure and Extinction of Strained Premixed Flames: Part I- Moderate Rates of Rotation," *Phys. Fluids A*, Vol. 2, No. 7, pp. 1213-1222.
- Maxey, R. M., and Riley, J. J., 1983, "Equation of Motion for a Small Rigid Sphere in a Nonuniform Flow," *Phys. Fluids*, Vol. 26, pp. 883-889.
- Odar, F., and Hamilton, W. S., 1964, "Forces on a Sphere Accelerating in a Viscous Fluid," *J. Fluid Mech.*, Vol. 18, pp. 302-314.
- Odar, F., 1966, "Verification on the Proposed Equation for Calculation of the Forces on a Sphere Accelerating in a Viscous Fluid," *J. Fluid Mech.*, Vol. 25, pp. 591-592.
- Odar, F., 1968, "Unsteady Motion of a Sphere Along a Circular Path in a Viscous Fluid," *J. Applied. Mech.*, Vol. 90, pp. 652-654.
- Oseen, C. W., 1927, *Hydrodynamik*. Leipzig: Akademische Verlagsgesellschaft.
- Putnam, A., 1961, "Integrable Form of Droplet Drag Coefficient," *ARS J.* 31: 1467-68.
- Puri, I. K., and Libby, P. A., 1990, "On the Forces of Droplets in Poiseuille Flow," *Phys. Fluids A*, Vol. 2, No. 7, pp. 1281-1284.
- Puri, I. K., and Libby, P. A., 1989, "Droplet Behavior in Counterflowing Streams," *Combust. Sci. and Tech.*, Vol. 66, pp. 267-292.
- Saffman, P. G., 1965, "The lift on a Small Sphere in a Slow Shear Flow," *J. Fluid Mech.*, Vol. 22, pp. 385-400.
- Temkin, S., and Kim, S. S., 1980, "Droplet Motion Induced by Weak Shock Waves," *J. Fluid Mech.*, Vol. 96, pp. 133-157.
- Temkin, S., and Mehta, H. K., 1982, "Droplet Drag in an Accelerating and Decelerating Flow," *J. Fluid Mech.*, Vol. 116, pp. 297-313.
- Tsuji, Y., Kato, N., and Tanaka, T., 1990, "Experiments on the Unsteady Drag and Wake of a Sphere at High Reynolds Number," *J. Multiphase Flow*, Vol. 17, No. 3, pp. 343-354.

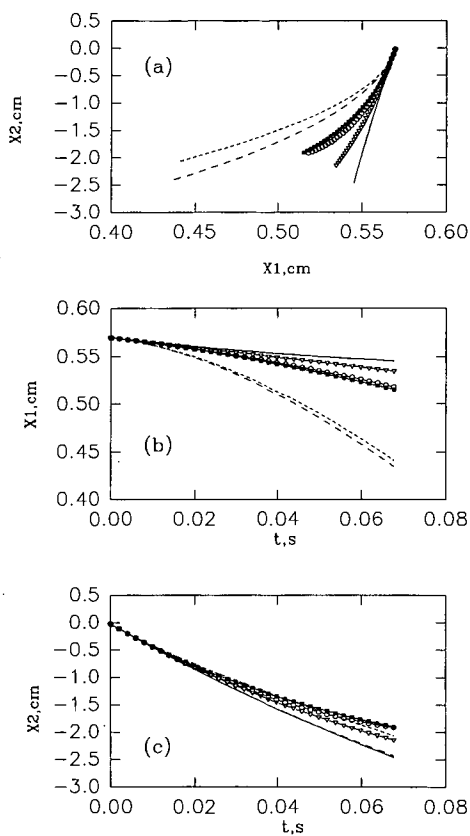


FIGURE 1 Droplets in Poiseuille flow : case 1

- (a) Trajectories.
- (b) Displacement histories in radial direction.
- (c) Displacement histories in axial direction.

--- Approach 1	----- Approach 2	▼ Approach 3
- - - Approach 4	— Approach 5	• Exp. data

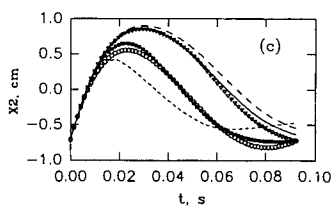
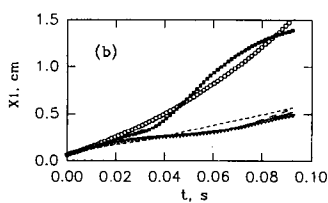
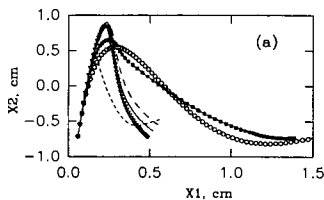
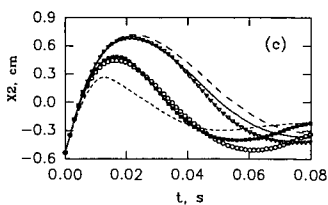
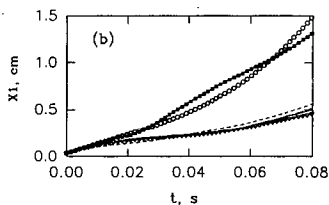
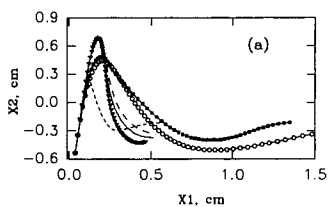


FIGURE 2 Droplets in counterflow : $Dd=100E-6$ (m) FIGURE 3 Droplets in counterflow : $Dd=130E-6$ (m)

- (a) Trajectories.
(b) Displacement histories in radial direction.
(c) Displacement histories in axis direction.

--- Approach 1 - - - - Approach 2 * Approach 3
• Approach 4 — Approach 5 • Exp. data

EFFECTS OF MARANGONI CONVECTION ON TRANSIENT DROPLET EVAPORATION IN REDUCED GRAVITY

H. Niazmand, B. D. Shaw, and H. A. Dwyer
Mechanical, Aeronautical and Materials Engineering Department
University of California
Davis, CA 95616

Keywords: Droplet Vaporization, Marangoni, Thermocapillary

INTRODUCTION

Because of its practical and fundamental importance, droplet vaporization, with its complicating features of surface regression, surface blowing, and transient energy and species diffusion, has been the subject of a large number of experimental, analytical and computational studies over the timespan of several decades. A literature review has revealed, however, that previous studies of droplet gasification have generally neglected effects of surface-tension gradients. The only related study that has been found is that of Higuera and Liñán¹, which is a linear stability analysis of an unsupported and stationary droplet vaporizing in a hot stagnant atmosphere. Here we present a computational study of the effects of Marangoni (thermocapillary) convection on transient temperature and velocity profiles in octane or methanol droplets vaporizing in a hot environment. Large and small droplets (initial diameters of 2 mm and 100 μm) are considered, and gravity is neglected. The large-droplet calculations are most applicable to reduced-gravity droplet experiments, while the small-droplet calculations are relevant to practical sprays.

Marangoni convection is induced by surface-tension variations along an interface between two fluids. The surface tension variations are caused by temperature gradients parallel to the interface. Since an interface has negligible thickness, surface-tension gradients must be balanced by viscous shear stresses on either side of the interface. If viscous stresses are large relative to surface-tension gradients, thermocapillary effects may be neglected. However, when viscous stresses and surface-tension gradients are comparable, thermocapillary effects are likely very important; this is the situation encountered in thermocapillary migration of droplets and bubbles in temperature gradients. Studies of thermocapillary migration have typically not considered the effects of phase changes, surface regression, surface blowing, or transient energy and species diffusion.

Estimates of the importance of capillary effects on droplet vaporization may be made by considering a droplet of radius r moving with the speed U_∞ relative to a gaseous environment. An average shear stress acting on the droplet from the gas side may be defined as $\rho_\infty U_\infty^2 C_D/2$, where ρ_∞ is the ambient gas density and C_D the drag coefficient. This shear stress will induce convection in the droplet interior. A temperature gradient along the liquid surface will produce an average surface-tension gradient $\Delta\sigma/r$ (σ is surface tension) that will be balanced by surface shear stresses in the gas and liquid phases. We may characterize $\Delta\sigma$ as $\sigma_T \Delta T$, where T is temperature, $\sigma_T = |\partial\sigma/\partial T|$, and ΔT the temperature difference from one side of the droplet to the other. Surface tension gradients will not significantly affect liquid convection processes if $\Delta\sigma/r$ is significantly less than $\rho_\infty U_\infty^2 C_D/2$. In terms of temperature differences, thermocapillary effects should be small if $\Delta T \ll (\rho_\infty U_\infty^2 C_D)/\sigma_T$. We may introduce the droplet Reynolds number $Re = 2rU_\infty\rho_\infty/\mu_\infty$, where μ_∞ is the ambient viscosity, to yield $\Delta T \ll C_D\mu_\infty^2 Re^2/(4r\sigma_T\rho_\infty)$. Consider a 2 mm diameter hydrocarbon droplet in 1000 K air at 1 atm. If $Re = 10$, $C_D = 1$, and $\sigma_T = 10^{-4} \text{ N/(m}^2\text{K)}$ (a value appropriate for hydrocarbon or methanol droplets at subcritical conditions^{2,3}), we find that $\Delta T \ll 1 \text{ K}$ is required for surface tension gradients to be negligible. For $Re = 0.1$ (and $C_D \approx 24/Re$), it is required that $\Delta T \ll 0.01 \text{ K}$. Hence, even modest temperature differences may induce significant thermocapillary forces. It is thus desirable to investigate in more detail the effects of capillary

forces on droplets. To this end, a computational model for axisymmetric droplet vaporization, including surface-tension gradients, was developed and is presented below.

EQUATIONS AND METHODS OF APPROACH

In this paper we started from the low Mach number model of the Navier-Stokes equations in control volume form. This model eliminates acoustic waves from the Navier-Stokes equations, and it will not be derived in the present paper. The equations for axisymmetric flow in control volume form are

Conservation of Mass

$$\frac{\partial}{\partial t} \iiint_V \rho dV + \oint_A \rho \mathbf{V} \cdot d\bar{\mathbf{A}} = 0$$

Momentum Equations

$$\iiint_V \rho \left[\frac{\partial}{\partial t} \mathbf{u} + \mathbf{V} \cdot \nabla \mathbf{u} \right] dV = - \oint_A P \bar{\mathbf{e}}_r \cdot d\bar{\mathbf{A}} + \oint_A \bar{\boldsymbol{\tau}} \cdot d\bar{\mathbf{A}}$$

$$\iiint_V \rho \left[\frac{\partial}{\partial t} \mathbf{v} + \mathbf{V} \cdot \nabla \mathbf{v} \right] dV = - \oint_A P \bar{\mathbf{e}}_\theta \cdot d\bar{\mathbf{A}} + \oint_A \bar{\boldsymbol{\tau}} \cdot d\bar{\mathbf{A}}$$

Thermal Energy Equation

$$\iiint_V \rho C_p \left[\frac{\partial T}{\partial t} + \mathbf{V} \cdot \nabla T \right] dV = \oint_A \lambda \nabla T \cdot d\bar{\mathbf{A}} - \iiint_V \rho \sum_{k=1}^K Y_k C_{p,k} \mathbf{V}_k \cdot \nabla T dV$$

Species Transport Equations

$$\iiint_V \rho \left[\frac{\partial Y_i}{\partial t} + \mathbf{V} \cdot \nabla Y_i \right] dV = \oint_A \rho D_i \nabla Y_i \cdot d\bar{\mathbf{A}}$$

Equation of State

$$P_T = \rho RT$$

where the following notation has been employed: ρ - is density; \mathbf{V} - fluid velocity; T - temperature; Y_i - mass fraction of species i ; and $\bar{\boldsymbol{\tau}}$ is the stress tensor in the fluid. The thermodynamic and transport properties for the gas and liquid have been obtained from Refs. [4-6]. At the interface location between the gas and liquid phases the conditions of continuity of heat flux, mass flux and tangential velocity have been employed, and the equilibrium condition of the Clausius-Clapeyron equation was used to determine the concentration of the liquid components in the gas phase at the interface. Tangential viscous stresses and surface-tension gradients were appropriately balanced at the interface. In addition, gravitational forces were assumed to be negligible.

The above system of equations has been solved numerically with a time accurate method, and with the use of a predictor/corrector method developed previously⁷. In general the addition of surface tension gradients has not caused any explicit change in the numerical methods; however the large surface velocities and gradients generated by surface tension effects have caused a need for smaller time steps to properly resolve the surface phenomena in time. The numerical calculations have been started from a uniform constant velocity initial condition in the gas, and a uniform zero velocity condition in the liquid. This condition, which is typical of droplet injection, causes a rapid buildup of the surface velocities as will be seen in the results section of the paper.

RESULTS

Calculations were performed for octane or methanol droplets in air at 1 atm. Initial droplet diameters and temperatures were taken in all cases to be 2 mm or 100 μm , and 300 K, respectively. Initial droplet Reynolds numbers of 0.1 and 10 were considered. For the $\text{Re} = 10$ calculations, vaporization in a 1000 K environment was allowed and the droplet-gas relative velocity was held constant. For $\text{Re} = 0.1$ vaporization in a 400 K environment was neglected, though droplets slowed down from drag.

Figure 1 shows the transient droplet surface velocity profiles for octane droplets (initially 2 mm) when surface-tension gradients are neglected. (Figures 1 and 2 are three-dimensional plots, with the height above a point in the "time-angle" plane representing the ratio U/U_∞ , where U_∞ is the local interface velocity). As would normally be expected, the surface velocities initially rapidly increase and then approach a steady-state condition. In Fig. 2, the same conditions are assumed, except that here thermocapillary effects are allowed. It is evident that that surface velocities are much larger in this case, especially near the beginning of the vaporization history. In each figure, the maximum time plotted is for the gas-phase time scale $\tau_g = \eta_{\infty}/(\rho_{\infty}r_0^2) = 24.86$, where r_0 is the initial droplet radius. In Fig. 1, the largest velocity ratio is $U/U_\infty = 0.036$, while in Fig. 2 the largest velocity ratio is $U/U_\infty = 0.086$.

Figures 3 and 4 show comparisons of droplet temperature profiles at $\tau_g = 24.86$ for octane and methanol droplets initially 2 mm in diameter. In each figure, the top half shows droplet isotherms when surface-tension gradients are accounted for (case 1), while the bottom half shows droplet isotherms when surface-tension gradients are neglected (case 2). The maximum and minimum temperatures for the isotherms drawn are listed in the figures. For each plot, the temperature difference between each isotherm is the same, though isotherm temperature differences vary between plots. For both fuels, thermocapillary forces significantly affect temperature fields.

Figures 5 and 6 show surface temperature profiles for octane droplets initially 2mm and 100 μm in diameter, respectively, at $\tau_g = 24.86$. Cases 1 and 2 correspond to vaporization with and without surface-tension gradients, respectively. In these figures, it is evident that allowing for thermocapillary effects significantly reduces surface temperature variations, especially for larger droplets. In essence, thermocapillary forces act to smooth out temperature gradients by inducing convective flows. Even though surface temperature variations are significantly reduced by thermocapillary effects, the associated thermocapillary flows are still very important. For example, Figs. 7 and 8 show the droplet surface velocity profiles (cases 1 and 2 are as defined above) for the same times listed for Figs. 5 and 6. Again, it is evident that thermocapillary effects significantly affect the velocity profiles. What is especially notable, though, is the prediction that surface-tension gradients tend to decrease droplet surface velocities. The reason for this can be inferred from Figs. 5 and 6, where it can be seen that, at the time shown, the octane droplets are coolest near the stagnation point (angular position of zero). Thermocapillary effects thus strongly oppose gas-phase shear stresses. As a result, surface-tension gradients significantly inhibit droplet internal convection (see also Figs. 3 and 4).

Figure 9 (which is to be interpreted in the same way as Figs 1 and 2) shows transient surface velocity profiles (the maximum time plotted is $\tau_g = 23.52$), while Fig. 10 gives surface velocity profiles at $\tau_g = 23.52$ for nonvaporizing 2 mm octane droplets subjected to heating in a 400 K environment. These calculations were done for an initial Re of 0.1 (the droplet velocity was allowed to decay from drag). Surface-tension gradients were allowed for the results given in Fig. 9. In Fig. 10, results are presented both including and neglecting thermocapillary effects (cases 1 and 2, respectively). A striking feature of Fig. 9 is the oscillatory nature of the velocity profiles. The maximum velocity ratio in Fig. 9 is $U/U_\infty = 0.126$. In Fig. 10, it is evident that thermocapillary forces significantly affect velocity profiles; even at this low Re , small surface temperature variations produce appreciable effects.

SUMMARY AND CONCLUSIONS

The calculations presented here demonstrate that thermocapillary effects may significantly influence droplet vaporization, especially during the early periods of a droplet's lifetime. Further work is required to more clearly quantify the effects of capillary forces (from temperature and/or composition variations along a droplet's surface) on droplet gasification phenomena.

ACKNOWLEDGEMENT

Financial support from NASA and the Daimler-Benz Corporation is gratefully acknowledged.

REFERENCES

1. Higuera, F. J. and Liñán, A., *Prog. Astro. Aero.* 105: p. 217 (1985).
2. Vargaftik, N. B., *Handbook of Physical Properties of Liquids and Gases*, 2nd ed., Hemisphere (1975).
3. Weast, R. C., *CRC Handbook of Chemistry and Physics*, 65th ed., CRC Press (1984).
4. Kee, R.J., Rupley, F.M., and Miller, J.A.: "Chemkin II: A Fortran Chemical Kinetics Package for the Analysis of Gas-Phase Chemical Kinetics", Sandia National Laboratories Report SAND89-8009 (1990).
5. Kee, R.J., Dixon Lewis, G., Warnitz, J., Coltrin, M.E. and Miller, J.A.: "A Fortran Computer Code Package for the Evaluation of Gas Phase Multicomponent Transport Properties", Sandia National Laboratories Report SAND86-8246 (1986).
6. Reid, R. C., Prausnitz, J. M., and Poling, B. E., *The Properties of Gases and Liquids*, 4th ed., McGraw-Hill (1987).
7. Dwyer, H.A., *Prog. Energy Combust. Sci.* 15, p. 131 (1989).

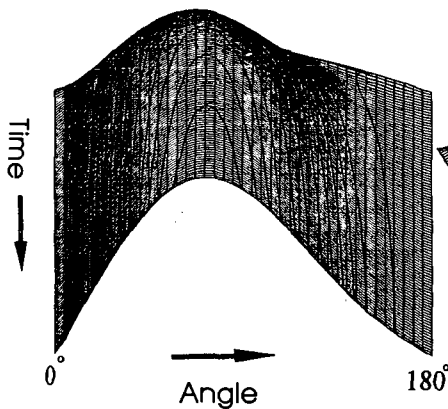


Figure 1. Surface velocity history for a vaporizing octane droplet without thermocapillary effects.

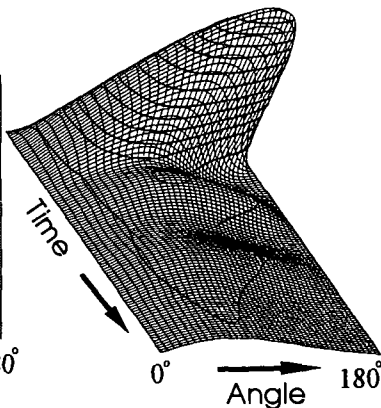
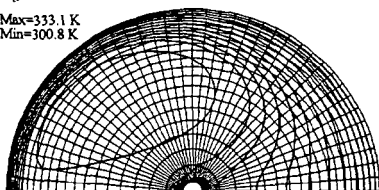


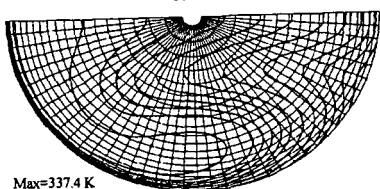
Figure 2. Surface velocity history for a vaporizing octane droplet with thermocapillary effects.

Max=333.1 K
Min=300.8 K



Case 1

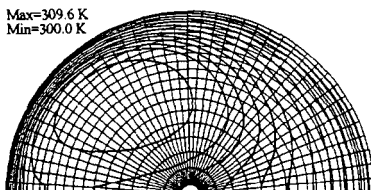
Case 2



Max=337.4 K
min=300.9 K

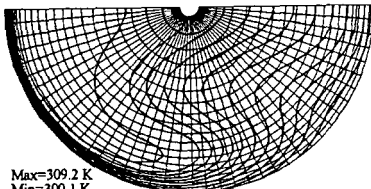
Figure 3. Interior temperature profiles of a vaporizing octane droplet with and without surface tension gradients.

Max=309.6 K
Min=300.0 K



Case 1

Case 2



Max=309.2 K
Min=300.1 K

Figure 4. Interior temperature profiles of a vaporizing methanol droplet with and without surface tension gradients.

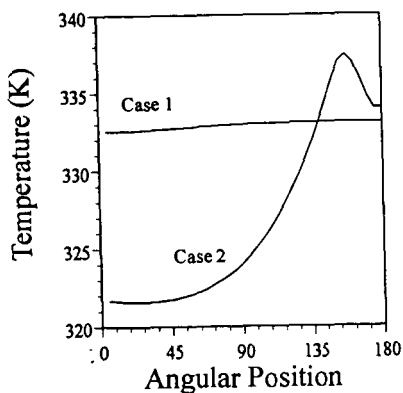


Figure 5. Comparison of surface temperature profiles of a vaporizing octane droplet.

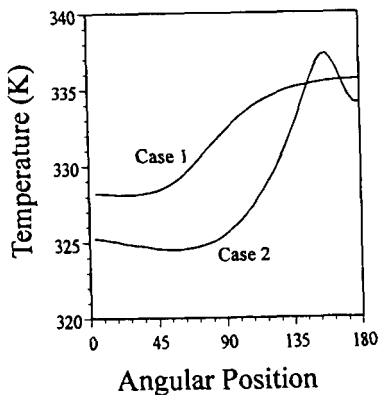


Figure 6. Comparison of surface temperature profiles of a vaporizing small octane droplet.

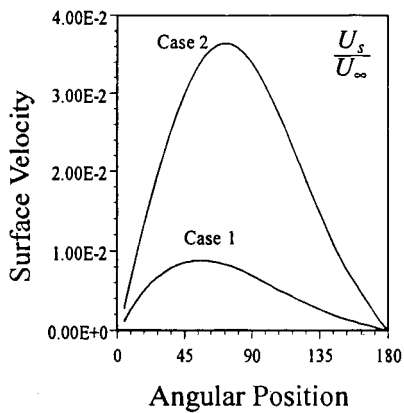


Figure 7. Comparison of surface velocity profiles of a vaporizing octane droplet.

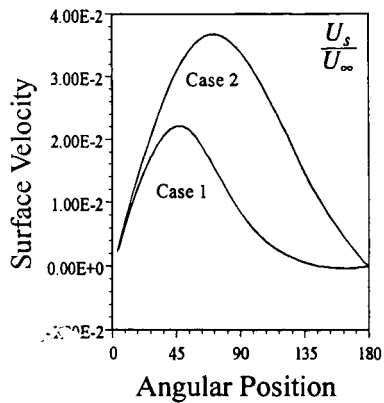


Figure 8. Comparison of surface velocity profiles of a vaporizing small octane droplet.

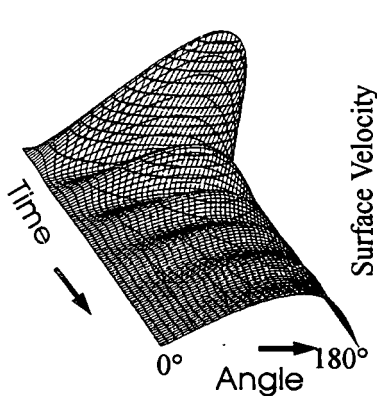


Figure 9. Surface velocity history of a nonvaporizing octane droplet at low Reynolds number with surface tension gradients.

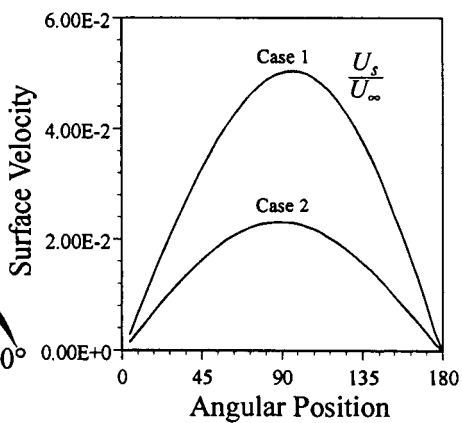


Figure 10. Comparison of surface velocity of an octane droplet at low Reynolds number.